Analyzing the Rydberg-based optical-metastable-ground architecture for ^{171}Yb nuclear spins

Neville Chen,[1,*] Lintao Li,[1,*] William Huie,[1,*] Mingkun Zhao,[1] Ian Vetter,[1] Chris H. Greene,[2,3] and Jacob P. Covey[1,†]

[1]*Department of Physics, The University of Illinois at Urbana-Champaign, Urbana, Illinois 61801, USA*

[2]*Department of Physics and Astronomy, Purdue University, West Lafayette, Indiana 47907, USA*

[3]*Purdue Quantum Science and Engineering Institute, Purdue University, West Lafayette, Indiana 47907, USA*

(Received 11 January 2022; revised 17 April 2022; accepted 12 May 2022; published 25 May 2022)

Neutral alkaline earth(like) atoms have recently been employed in atomic arrays with individual readout, control, and high-fidelity Rydberg-mediated entanglement. This emerging platform offers a wide range of new quantum science applications that leverage the unique properties of such atoms: ultranarrow optical "clock" transitions and isolated nuclear spins. Specifically, these properties offer an optical qubit (o) as well as ground (g) and metastable (m) nuclear spin qubits, all within a single atom. We consider experimentally realistic control of this *omg* architecture and its coupling to Rydberg states for entanglement generation, focusing specifically on ytterbium-171 (^{171}Yb) with nuclear spin $I = \frac{1}{2}$. We analyze the S-series Rydberg states of ^{171}Yb, described by the three spin-$\frac{1}{2}$ constituents (two electrons and the nucleus). We confirm that the $F = \frac{3}{2}$ manifold, a unique spin configuration, is well suited for entangling nuclear spin qubits. Further, we analyze the $F = \frac{1}{2}$ series, described by two overlapping spin configurations, using a multichannel quantum defect theory. We study the multilevel dynamics of the nuclear spin states when driving the clock or Rydberg transition with Rabi frequency $\Omega_c = 2\pi \times 200$ kHz or $\Omega_R = 2\pi \times 6$ MHz, respectively, finding that a modest magnetic field ($\approx$200 G) and feasible laser polarization intensity purity ($\lesssim$0.99) are sufficient for gate fidelities exceeding 0.99. We also study single-beam Raman rotations of the nuclear spin qubits and identify a "magic" linear polarization angle with respect to the magnetic field at which purely σ_x rotations are possible.

DOI: 10.1103/PhysRevA.105.052438

I. INTRODUCTION

Individually trapped neutral atoms with interactions mediated by highly excited Rydberg states have become a prominent platform for quantum science [1–3]. Most research to date with arrays of neutral atoms has been conducted with alkali-metal species, but alkaline earth(like) atoms (AEAs) are gaining prominence after bosonic ($I = 0$) [4–16] and fermionic ($I > 0$) [17–19] isotopes recently joined this field. AEAs offer qualitative differences and quantitative advantages over alkali metals. For example, they offer long-lived metastable states useful for applications including optical metrology [20]; high-fidelity, lossless, state-resolved detection via "shelving" [7–9]; and high-fidelity Rydberg-mediated entanglement [12,14,15].

Fermionic isotopes have two potential advantages over their bosonic counterparts: (1) their optical "clock" transition is significantly stronger due to hyperfine mixing [21], and (2) the ground and metastable "clock" states have a nuclear spin degree of freedom decoupled from electronic spin, which was recently utilized as a high-fidelity qubit [17–19]. These optical and nuclear degrees of freedom can be identically trapped at a "magic" wavelength [7,8,22] where coherence times approach the minute scale [13,17]. Such access to multiple highly coherent qubit types within a single atom may obviate the need for heterogeneous qubit architectures, which have become ubiquitous in myriad quantum science platforms [23–27]. We extend the term *omg* ("optical, metastable, and ground") from a recent trapped ion proposal [28] to describe neutral fermionic AEAs in this context.

Here, we analyze the Rydberg-based *omg* architecture for ^{171}Yb nuclear spins. We consider a "g" qubit $\{\downarrow_g, \uparrow_g\}$ encoded in the ground state $^1S_0$ and a "m" qubit $\{\downarrow_m, \uparrow_m\}$ encoded in the metastable clock state $^3P_0$ [see Fig. 1(a)]. These nuclear qubits can be manipulated by stimulated Raman transitions via other states [17,18], as is common for hyperfine qubits in neutral alkali-metal atoms [29] and trapped ions [28]. The "g" and "m" qubits are connected via the "o" qubit on the clock transition, and identical trapping conditions for all four states can be realized at the clock-magic wavelength of 759 nm where long coherence times are available [20,22]. We propose an architecture centered around the "m" qubit to leverage these degrees of freedom. We show that the combination of a modest magnetic field ($B \approx 200$ G) and optical polarization intensity purity ($\approx$99%) is sufficient to perform >0.99 fidelity operations on the nuclear qubits via the clock, Rydberg, and Raman transitions, approaching the fault-tolerance threshold [30,31]. We assume a coherence time of $T_2^* \approx 1$ s, limited by mG-level magnetic field noise (see Appendix D) as well as off-resonant scattering from the tweezer traps (see Appendix E). This decoherence rate ($\sim 2\pi \times 1$ Hz) can be compared to the limiting gate operation rate, the anticipated optical qubit Rabi frequency ($\Omega_c \approx 2\pi \times 200$ kHz), suggesting a promising platform for Rydberg-based

*These authors contributed equally to this work.

†jcovey@illinois.edu

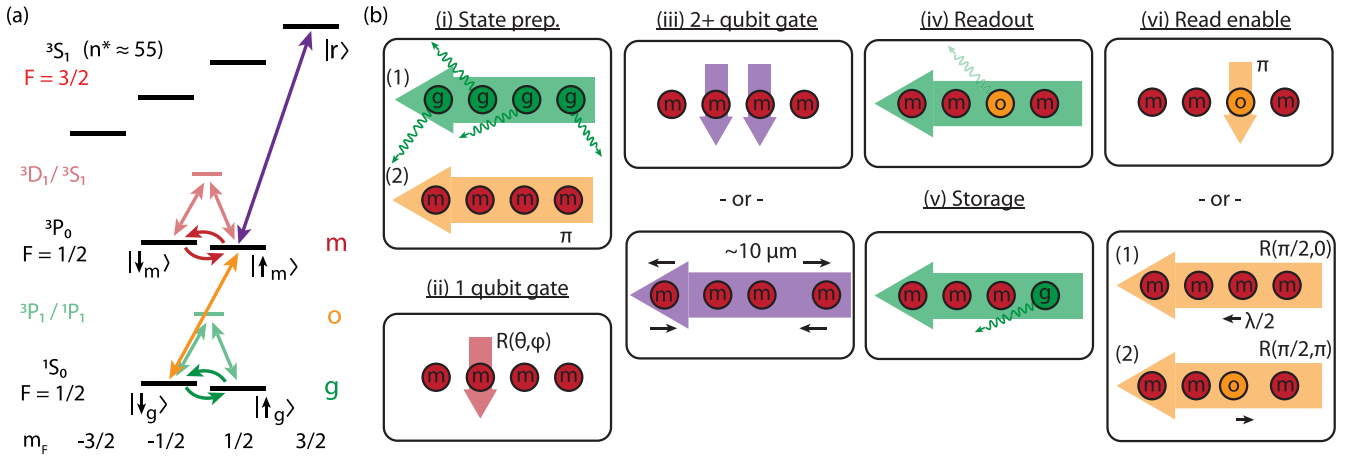

FIG. 1. Overview of the ^{171}Yb *omg* architecture. (a) The relevant level structure, showing the metastable ("*m*") and ground ("*g*") qubit encoded in the "clock" and ground states, respectively, as well as the "clock" (yellow arrow) and Rydberg (purple arrow) transitions. Qubit rotations can be performed with stimulated Raman processes via other, strong transitions (green and red arrows). (b) Overview of operations for "*m*" qubits. (i) State preparation begins with cooling and optical pumping (solid arrows are laser pulses and wiggly arrows are emitted photons) in the ground state via an auxiliary transition to $^1P_1$ or $^3P_1$ (green), followed by a global π pulse on the optical qubit transition (yellow). (ii) Qubit rotations of "*m*" qubits (red) are performed with stimulated Raman transitions via other states. (The case is identical for "*g*" qubits). (iii) Rydberg-mediated two-qubit gates (purple), where targeted operations can be achieved in two ways (see text). (iv) Global readout is performed with the "*o*" qubit, where only the "*g*" sector fluoresces (translucent green) from light resonant with the auxiliary transition (green). (v) The "*m*" qubit can be used for storage that is immune to operations on the "*g*" qubit, including readout or rotations. (vi) The "*m*" qubit must be mapped to the "*o*" qubit (yellow) to perform readout with state-dependent fluorescence. There are two ways to perform a targeted read enable operation (see text).

entanglement in quantum computers and simulators [32–36], networks [37,38], and optical clocks [39–41].

II. THE *omg* ARCHITECTURE

There are countless ways to use the *o*, *m*, and *g* qubits, and the optimal variant of the *omg* architecture depends critically on the application. For example, an optical atomic clock [20] with programmable entanglement [16] for achieving precision below the standard quantum limit [39–41] will primarily focus on the *o* qubit. In this work, we focus on an architecture centered around the *m* qubit for three reasons: (1) the clock state is well suited for high-fidelity, single-photon coupling to Rydberg states in the $^3S_1$ series [12,14,16], obviating the need for two-photon transitions limited by off-resonant scattering from the intermediate state [19,29]; (2) the clock state is well suited for shelving of quantum information during readout based on fluorescence from the ground state [7,42,43]; and (3) the clock state of Yb has strong, telecom-band transitions to the ^3D_J series that offer opportunities for quantum networking [37,38].

For concreteness and to motivate the following analysis, we focus on the operations shown in Fig. 1(b). The *m* qubit will be used for computation and storage. Qubits will be globally initialized by cooling and optical pumping in the ground state via $^1P_1$ or $^3P_1$ followed by a π pulse on the clock transition to generate a fiducial register in $|\uparrow_m\rangle$. Rotations of *m* qubits will be performed with single-beam [18] stimulated Raman transitions via $^3S_1$ or $^3D_1$, which can be applied at the individual-qubit level via a tightly focused beam [17] (see Appendix J for an assessment of technical challenges with tightly focused beams). Two-qubit and multiqubit gates will be performed by coupling $|\uparrow_m\rangle$ to a Rydberg state $|r\rangle$, which can be applied at the individual-qubit level with tightly focused beams to drive the transition [44] or Stark-shift individual sites [15,19], or with coherent transport techniques based on the $1/r^6$ scaling of the Rydberg-Rydberg interactions that map proximity onto connectivity [45–47]. Although the latter approach excites all qubits to $|r\rangle$ which introduces a larger error rate, the use of only global pulses offers an elegant simplicity. Lossless, state-resolved readout is performed by mapping qubits to the *o* type and then collecting fluorescence from the ground state via its transition to $^1P_1$ or $^3P_1$ [7,8,12,17]. Fluorescence in the *g* manifold does not affect quantum information in the *m* manifold, and thus storage in *m* enables parallel processes in *g* such as single-qubit readout [42,43] and remote entanglement generation [38].

Control of the *o* qubit plays a crucial role for type-casting and read enabling. Single-qubit, mid-circuit readout requires a π pulse on the clock transition to be performed at the individual qubit level. This can be accomplished with a tightly focused beam or with a global [8,9], two-component pulse combined with coherent transport of the target qubit. Specifically, this technique would leverage the spatial variation of the optical phase combined with the ability to move a single atom by half a wavelength, corresponding to a π-phase shift, to perform a net 1π pulse on the target atom and a net 0π pulse on the spectator atoms [48,49]. While we leave further analysis of this approach for future work, we note that the spatial precision available with adaptive optical elements such as acousto-optic deflectors (AODs) is sufficient. Typical AOD-based tweezer systems have a position-to-radio-frequency (rf) conversion of $\approx$10 μm/MHz [7,50], and thus the $\approx$10 nm precision required for this protocol to be performed with a fidelity at the 0.99 fidelity level corresponds to only kHz-level precision of the rf signals.

III. RYDBERG TRANSITION

We now discuss the required operations of this architecture in detail, beginning with the Rydberg-based operations. Inspired by recent work [12,14,16], we consider Rydberg-mediated entanglement via the $^3P_0 \leftrightarrow {}^3S_1$ transition, where the latter has a principal quantum number of $n \approx 60$ [see Fig. 1(a)]. However, we note that a two-photon transition from the $^1S_0$ ground state could be used instead [10,15,19,51] at the expense of higher optical power and additional complexity, and was recently used to perform two-qubit gates on the nuclear spin qubit in the ground state of ^{171}Yb at low field (≈4 G) [19]. We require a protocol by which only one of the qubit states couples to the Rydberg level [29,52]. Although we specifically consider the m qubit, the requirements on the isolation of the Rydberg drive from unwanted "spectator" states is stringent for all qubit choices. The nuclear spins present a unique challenge due to their relatively small energy splittings (≈kHz/G). Hence, the development of a high-fidelity two-qubit or mutliqubit gate protocol for fermionic AEAs will require a detailed understanding of the Rydberg level structure [19,51,53–55]. We use multichannel quantum defect theory [56] (see Appendix A) to gain new insight on this structure. We consider S-series Rydberg states ($L = 0$), but our analysis can be applied to $L > 0$.

The presence of a nuclear spin in an AEA creates a scenario that is qualitatively different from both alkali-metal and bosonic AEA Rydberg structures. In the case of alkali-metal species, the electron-nucleus coupling is small due to the large orbit of the Rydberg electron, and thus the total electron angular momentum J is a good quantum number. In the case of bosonic AEAs, there are two electron spins but no nuclear spin, so electron total spin S (i.e., singlet and triplet) and J are good quantum numbers. Fermionic AEAs present a system in which there are three coupled spins: two electrons and a nucleus. Indeed, the hyperfine structure of the ionic core describes the Rydberg ionization thresholds [see Fig. 2(a)]. The Rydberg series corresponding to total angular momentum $F = \frac{1}{2}$ is not well described by $S_{\rm tot}$, meaning that the singlet or triplet designation is inappropriate since two configurations ($f_c = 0$ and 1) both contribute, and a multichannel quantum defect theory [56] is required. Conversely, the series corresponding to $F = \frac{3}{2}$ can only be obtained from one configuration ($f_c = 1$) and is thus well described by $S_{\rm tot} = 1$. Due to its clean structure for all n (assuming no perturbers) and its designation as a "spin triplet," we target this $F = \frac{3}{2}$ series as being ideally suited for our two-qubit or multiqubit entangling operations [19].

Figures 2(b) and 2(c) show the spectrum of the $F = \frac{1}{2}$ and $\frac{3}{2}$ series of the S manifold at low principal quantum number n and effective principal quantum number near $n^* \approx 55$, respectively. In the small-n limit [57], the singlet-triplet splitting is much larger than the hyperfine splitting of $F = \{\frac{1}{2}, \frac{3}{2}\}$ in the $^3S_1$ manifold (≈10 GHz [57]). Near $n^* = 55$, the two configurations of $F = \frac{1}{2}$, analyzed with multichannel quantum defect theory [56] (see Appendix A), follow the same trend line before separating to asymptotically approach the $f_c = \{0,\ 1\}$ limits [see Fig. 2(a)]. The $F = \frac{3}{2}$ series has only a single configuration asymptotically approaching $f_c = 1$. The state energies in this series can thus be modeled using the known energies of the $^3S_1$ series in the bosonic isotope ^{174}Yb

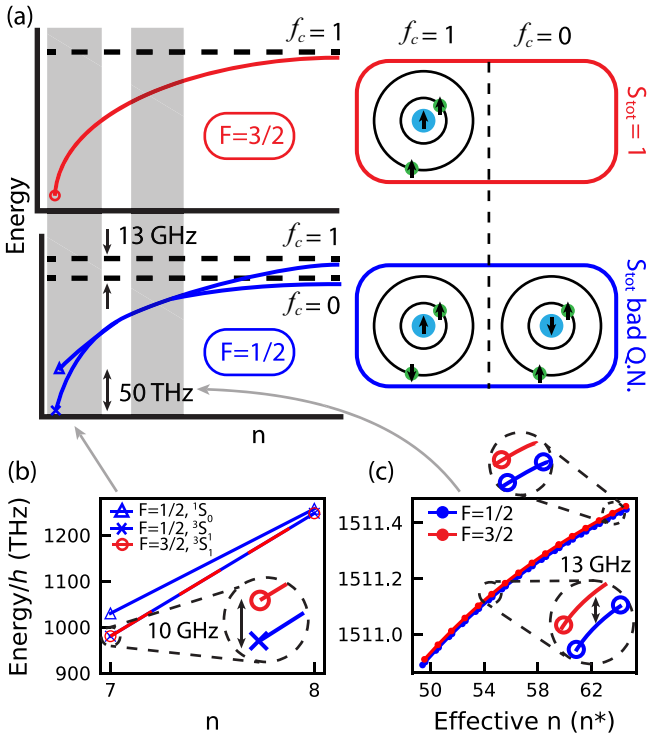

FIG. 2. The S-series Rydberg structure of ^{171}Yb. (a) The energy levels and spin configurations of the two S series described by total angular momentum $F = \{\frac{1}{2}, \frac{3}{2}\}$ versus principal quantum number (n). They asymptotically approach the hyperfine levels of the core ion $f_c = \{0,\ 1\}$ split by 12.6 GHz. The $F = \frac{3}{2}$ series is uniquely described by $S_{\rm tot} = 1$ since all three spins must be aligned. The $F = \frac{1}{2}$ series results from two configurations of the three spins, so $S_{\rm tot}$ is not a good quantum number in this case. (b) The two series at small n, where the hyperfine splitting of the $^3S_1$ term into $F = \{\frac{1}{2}, \frac{3}{2}\}$ is smaller than the singlet-triplet splitting. (c) The two series at $n^* \approx 50$–65 ($n \approx 55$–70) using multichannel quantum defect theory for the $F = \frac{1}{2}$ series. The lower inset shows a separation of $\approx\Delta_{\rm HFS}$ between the two series at $n^* \approx 55$, while the upper inset shows a near degeneracy at $n^* \approx 65$.

(obtained from Ref. [10]) plus the hyperfine splitting $\Delta_{\rm HFS} = 2\pi \times 12.6$ GHz of the ^{171}Yb ionic core (see Appendix B). Figure 2(c) shows both the $F = \frac{1}{2}$ and $\frac{3}{2}$ series near $n^* = 55$, where the figure of merit is the energy separation between the two series and the associated resolvability of a given state. Near $n^* = 55$ (lower inset), the ≈13 GHz separation of the states in the $F = \frac{3}{2}$ series from the closest ones in the $F = \frac{1}{2}$ series suggests excellent isolation in the presence of strong laser coupling. However, there are near degeneracies between the two series, such as near $n^* = 65$ (upper inset), that must be avoided. This is quantified more precisely by Lu-Fano plots [58] of the two series (see Appendix A).

We consider the use of the σ^+-polarized "stretched" transition between $^3P_0$ $|m_F = \frac{1}{2}\rangle \equiv |\uparrow_m\rangle$ and $^3S_1$ ($n \approx 60$) $|m_F = \frac{3}{2}\rangle \equiv |r\rangle$ [see Fig. 3(a)] to obviate the coupling with $|\downarrow_m\rangle$ in the presence of a slight polarization impurity [dashed arrows in Fig. 3(a)]. (See Appendix H for analysis of the π-polarized case.) The nature of the $F = \frac{3}{2}$ series allows for the standard Landé g factors to be used to compute Zeeman

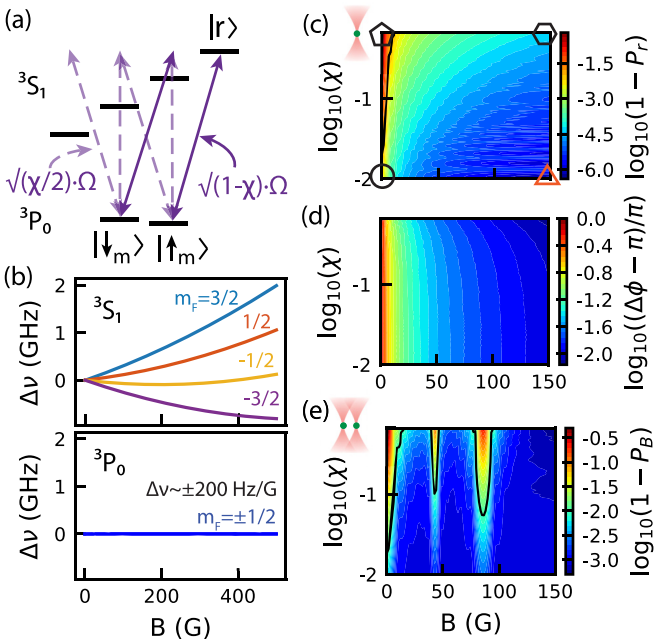

FIG. 3. Analysis of the Rydberg transition. (a) The six-level system showing the nuclear qubit $\{\downarrow_m, \uparrow_m\}$ in the clock state and the four m_F states in the $F = \frac{3}{2}$ Rydberg state. We target the σ^+ "stretched" transition $|\uparrow_m\rangle \leftrightarrow |r\rangle$, but imperfect polarization creates off-resonant couplings to other states. We parametrize the strengths of these couplings with $\sqrt{\chi/2}$ since polarization intensity purity is associated with optical power P, and $\Omega \sim \sqrt{P}$. Weighting by Clebsch-Gordan coefficients is included. (b) The magnetic field maps of the clock (including hyperfine interaction [21]) and Rydberg (including the diamagnetic shift [12]) states. (c) Single-atom π-pulse infidelity, initialized in $|\uparrow_m\rangle$, under various polarization impurities χ and magnetic fields B. The color scale is the population not in $|r\rangle$, $1 - P_r$. The shapes indicate the conditions under which Rabi oscillations are shown in Fig. 4. (d) Single-atom relative phase accrual on the $\{\downarrow_m, \uparrow_m\}$ qubit resulting from a 2π pulse on the $|\uparrow_m\rangle \leftrightarrow |r\rangle$ transition under various χ and B. The color scale shows the phase accrual in units of π radians, where π is expected in the ideal case. (e) Two-atom π-pulse infidelity, initialized in $|\uparrow_m\uparrow_m\rangle$, under various χ and B. The color scale is the population not in the $|B\rangle$ Bell state P_B (see text). The black lines in (c) and (e) show where $P = 0.99$.

splittings. We find $\Delta_Z/(2\pi) = m_F \times 1.9$ MHz/G in the low-field limit and we include the well-known [12] m_F-independent diamagnetic interaction $\Delta_{\rm DM} \sim |\mathbf{d} \times \mathbf{B}|^2$ that dominates at $B \gtrsim 800$ G. We neglect hyperfine mixing between Rydberg manifolds as there is no significant contribution for the conditions considered here (see Appendix B). The magnetic field shifts of the Rydberg states and the $^3P_0$ clock states are shown in Fig. 3(b).

To assess the prospect of gate operations on the $|\uparrow_m\rangle \leftrightarrow |r\rangle$ transition, we numerically simulate a drive of strength $\Omega_R = 2\pi \times 6$ MHz on the six-level system (see Appendix D) for various magnetic fields B and polarization intensity impurities χ [defined in Fig. 3(a)]. We assume magnetic field magnitude and orientation uniformity at the 10^{-4} level in a well-designed Helmholtz field [59,60]. This value of Ω_R was chosen based on similar work with global Rydberg pulses for strontium [12]; tightly focused pulses would require less power, albeit

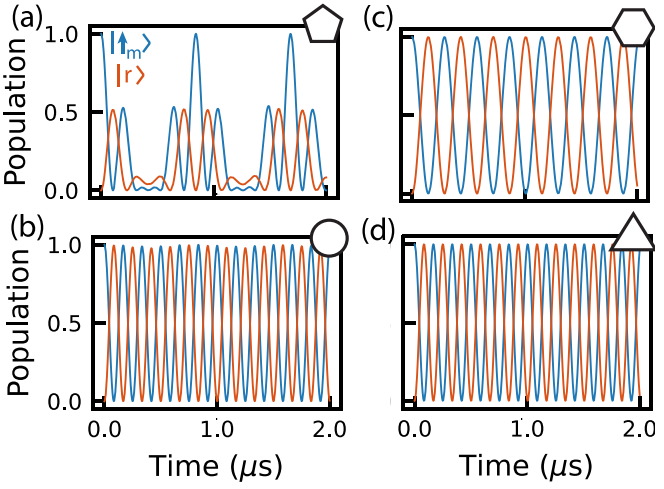

FIG. 4. Single-atom Rydberg Rabi oscillations. Populations $|\uparrow_m\rangle$ (blue) and $|r\rangle$ (orange) versus time under various χ and B conditions. Note that population is not conserved due to leakage to other states in the six-state system when $\chi > 0$. (a) $\chi = \frac{2}{3}$ (fully unpolarized) and $B = 0$ G. (b) $\chi = 10^{-2}$ and $B = 0$ G. (c) $\chi = \frac{2}{3}$ and $B = 150$ G. (d) $\chi = 10^{-2}$ and $B = 150$ G. Note that dephasing mechanisms (see text) are not included to avoid obfuscating the atomic structure considerations.

with added technical challenges (see Appendix J). The π-pulse infidelity (population not in $|r\rangle$, $1 - P_r$) for a single atom is shown in Fig. 3(c), where even 90% polarization intensity purity ($\chi = 10^{-1}$) at $B \approx 10$ G gives a transfer fidelity of $\mathcal{F} \approx 0.99$. The shapes included in Fig. 3(c) denote the plots in Fig. 4 showing Rabi oscillations during a prolonged pulse under those conditions.

We also consider the accrued relative phase on the $\{\downarrow_m, \uparrow_m\}$ qubit due to the undesired couplings during a $|\uparrow_m\rangle \leftrightarrow |r\rangle$ pulse. Although finite-phase accrual due to light shifts during gates can be tolerated, fluctuations in this phase due to, e.g., intensity fluctuations can have deleterious effects on the quantum circuit. To obviate this problem, it is clearly optimal to minimize the phase accrual due to parasitic couplings. To probe this effect in our system, we consider the accrued phase during a 2π pulse on $|\uparrow_m\rangle \leftrightarrow |r\rangle$ (see Appendix D3) for various magnetic fields and polarization intensity impurities [Fig. 3(d)]. We find that the accrued phase relative to the ideal case with zero coupling to other Rydberg states is $\Delta\phi \lesssim 0.01\pi$ for $B \gtrsim 150$ G for a wide range of χ. Percent-level fluctuations in this phase are negligible, and the phase itself is expected to be sufficiently small for a fidelity approaching 0.99 in intolerant applications.

Finally, we consider the prospects for two-qubit entanglement. Although we are interested in entanglement of low-lying states such as $\{\downarrow_m, \uparrow_m\}$ via protocols such as in Refs. [16,29,52,61], we consider only the $\{\uparrow_m, r\}$ qubit here since operation of this transition is required in any protocol and thus presents a fidelity limit. We look at the pulse fidelity in the two-atom case, assuming $C_6(n^* = 55) \approx 300$ GHz μm^6 based on recently measured values [19] that give a Rydberg interaction shift $U_{\rm vdW}/\hbar \approx 2\pi \times 160$ MHz ($\approx 27\Omega$) for an interatom separation of $r = 3.5$ μm, deep within the Rydberg blockade limit. We consider the entangled "bright"

Bell state $|B\rangle \equiv (|\uparrow_m r\rangle + |r \uparrow_m\rangle)/\sqrt{2}$, where the two elements in the state refer to the two atoms [12,62]. We study the population not in $|B\rangle$, $1 - P_B$, after a π pulse from $|\uparrow_m \uparrow_m\rangle$ to $|B\rangle$ for various magnetic fields and polarization intensity purities [Fig. 3(e)]. Resonances with the Rydberg states $|\{r_\Downarrow, r_\downarrow, r_\uparrow\}\rangle \equiv |m_F = \{-\frac{3}{2}, -\frac{1}{2}, +\frac{1}{2}\}\rangle$ occur at magnetic fields where $U_{\mathrm{VdW}} = [\Delta_z(m_F = \frac{3}{2}) - \Delta_z(m_F)] \times B$. The resonances corresponding to $|r_\downarrow\rangle$ and $|r_\uparrow\rangle$ manifest in Fig. 4(e) as regions with low pulse fidelity, exacerbated by high χ, while the resonance with $|r_\Downarrow\rangle$ is not apparent only because the initial state $|\uparrow_m \uparrow_m\rangle$ does not couple to it. This effect is irrelevant at fields of $B \gtrsim 200$ G that we later identify as optimal, and can be entirely removed by instead driving the $|\downarrow_m\rangle \leftrightarrow |r_\Downarrow\rangle$ (σ^+) transition since $U_{\mathrm{VdW}} > 0$.

This analysis suggests that our nuclear spin qubit is a viable platform for quantum science with Rydberg states, enabling two-qubit entanglement and many-body dynamics at or beyond the current fidelity record [12,14,29,63]. We briefly consider in Appendix K the well-known limitations to coherent Rydberg excitation: laser frequency noise, finite Rydberg state lifetime, dc Stark and Zeeman shifts, and random Doppler shifts due to finite atom temperature. There are also challenges associated with individual-qubit addressing [17,44], which we consider in Appendix J. However, these technical limitations are ubiquitous across species and qubit encodings and are thoroughly addressed elsewhere [10,12,62,64], but some are perhaps easier to mitigate with AEAs due to their access to higher Rydberg-excitation Rabi frequencies and colder temperatures [12,15,16,18]. The point of this analysis is rather to demonstrate that the entanglement of nuclear spin qubits is not limited by atomic structure under the correct conditions.

IV. CLOCK TRANSITION

We now turn to a discussion of the optical clock transition. As discussed above, global clock pulses are needed for initialization in the m qubit. Also, targeted clock operations for read enabling can be performed with either tightly focused clock beams, or potentially with global pulses combined with targeted position shifts [48,49]. For the purposes of this discussion, the most important parameters are the Rabi frequency Ω_c and the trapping frequency ω along the k vector of the clock pulse. In either case we assume $\Omega_c \approx 2\pi \times 200$ kHz is realistic (see Appendix E), which naturally requires more optical power in the global addressing case. Specifically, based on the well-known transition strength [65], $P = 50$ mW would be required for a beam of waist radius $w_0 = 20$ μm aligned along a one-dimensional array [8,9]. The relevant level structure is shown in Fig. 5(a). We again choose to drive a σ^+-transition to limit the possible undesired couplings. The Zeeman energies of the nuclear states are shown in Fig. 5(b), where hyperfine interactions affect the trend in the $^3P_0$ state. The differential g factor at low field is $\approx$200 Hz/G (see Appendix C), so we are reliant on polarization selectivity since the drive bandwidth will exceed the energy separation.

We analyze a π pulse of the clock transition, initialized in $|\downarrow_g\rangle$, for various polarization intensity purities and magnetic fields. In Appendix F, we consider phase noise since it constitutes a liability unique to optical qubits. However, we neglect phase noise here to avoid obfuscating the internal

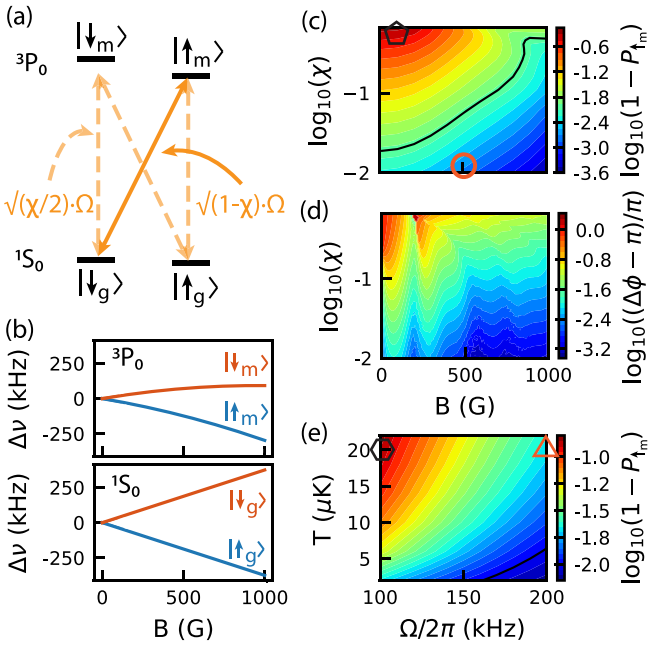

FIG. 5. Analysis of the clock transition. (a) The four-level system showing the nuclear qubits $\{\downarrow_g, \uparrow_g, \downarrow_m, \uparrow_m\}$ in the ground and clock states. We target the σ^+ "stretched" transition $|\downarrow_g\rangle \leftrightarrow |\uparrow_m\rangle$, but imperfect polarization creates off-resonant couplings to other states. We parametrize this identically to the Rydberg case in Fig. 3. (b) The magnetic field maps of the ground and clock states (including hyperfine interaction [21]). (c) π-pulse infidelity, initialized in $|\downarrow_g\rangle$, under various χ and B. The shapes indicate the conditions under which Rabi oscillations are shown in Fig. 6. The color scale is the population not in $|\uparrow_m\rangle$, $1 - P_{\uparrow_m}$, and the black line shows where $P_{\uparrow_m} = 0.99$. (d) Relative phase accrual on the $\{\downarrow_g, \uparrow_g\}$ qubit resulting from a 2π pulse on the $|\uparrow_g\rangle \leftrightarrow |\downarrow_m\rangle$ transition under various χ and B. The color scale shows the phase accrual in units of π radians, where π is expected in the ideal case. (e) Infidelity at $B = 500$ G due to finite-temperature effects in the four-level system (not including phase noise). $1 - P_{\uparrow_m}$ versus temperature and Rabi frequency. The shapes refer to Fig. 6.

dynamics and to keep the results general. Figure 5(c) shows the population not in $|\uparrow_m\rangle$, $1 - P_{\uparrow_m}$, and we find that a field strength of $B \gtrsim 200$ G with $\chi \gtrsim 10^{-2}$ polarization intensity purity is sufficient for population transfer exceeding 0.99. As a more stringent requirement than the π-pulse fidelity, we again consider relative phase accrual, now on the $\{\downarrow_g, \uparrow_g\}$ qubit, resulting from undesired couplings (see Appendix D3). Specifically, we consider a 2π pulse on the $|\downarrow_g\rangle \leftrightarrow |\uparrow_m\rangle$ transition. We find a relative phase accrual of $\Delta\phi \lesssim 0.01\pi$ for $B \gtrsim 200$ G and $\chi \gtrsim 10^{-2}$, sufficient for operations with a fidelity of $\gtrsim$0.99.

Finally, the analysis in Figs. 5(c) and 5(d) was performed without considering motional degrees of freedom. We now consider finite-temperature and atomic motion effects. For concreteness, we now assume a global pulse with k vector along the radial direction of the tweezer traps. In Appendix J, we consider pulses propagating in the axial direction, where the performance in this respect is improved due to the larger disparity between Ω_c and ω. Other technical challenges naturally emerge, however (see Appendix J). We assume a radial

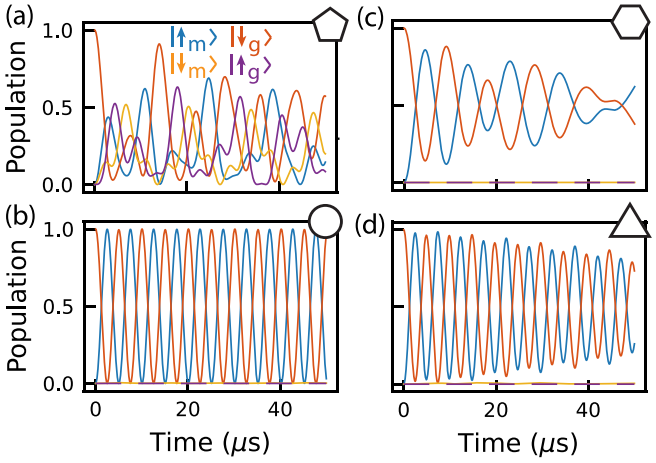

FIG. 6. Clock Rabi oscillations. The population in $|\uparrow_m\rangle$ (blue) and $|\downarrow_g\rangle$ (orange) versus time under various χ and B conditions. Note that population in these two states is not conserved as it leaks to $|\uparrow_g\rangle$ (purple) and $|\downarrow_m\rangle$ (yellow) when $\chi > 0$. (a) $\chi = \frac{2}{3}$, $B =$ 100 G, and $\Omega/2\pi = 200$ kHz; no motion. (b) $\chi = 10^{-2}$, $B = 500$ G, and $\Omega/2\pi = 200$ kHz; no motion. (c) $\chi = 10^{-2}$, $B = 500$ G, and $\Omega/2\pi = 100$ kHz; with motion ($T = 20\ \mu$K). (d) $\chi = 10^{-2}$, $B =$ 500 G, and $\Omega/2\pi = 200$ kHz; with motion ($T = 20\ \mu$K).

trap frequency in the tweezer of $\omega_r = 2\pi \times 70$ kHz (corresponding to a tweezer with $1/e^2$ waist radius of 700 nm and depth of 500 μK), which is significantly smaller than the Rabi frequency $\Omega_c = 2\pi \times 200$ kHz. These trap conditions correspond to a Lamb-Dicke parameter of $\eta_r = 0.22$, where $\eta = kx_0$ depends on the wave number k of the driving laser and the harmonic oscillator length $x_0 = \sqrt{\hbar/(2m_{\mathrm{Yb}}\omega_r)}$ of the atom in the trap. In the $\Omega_c \gg \omega_r$ limit with "magic" trapping conditions (under which the trap frequencies in the ground and clock states are equal [7,22]), we choose the basis states [18,66] to be $|g, n\rangle = |g\rangle \otimes |n\rangle$ and $|e, \xi(n)\rangle = |e\rangle \otimes e^{i\eta(\hat{a}+\hat{a}^\dagger)}|n\rangle$, where g (e) is the electronic ground (excited) state and n is the motional quantum number. We perform this analysis with all four states in the ground-clock manifold, but only list two here for brevity. This basis greatly simplifies the calculation for the case of a strong driving field since the Hamiltonian becomes sparse. See Appendix G for details.

At $B = 500$ G and $\chi = 10^{-2}$, we study the dependence of the π-pulse fidelity on temperature over the range of $T \in [2, 20]\ \mu$K (where temperatures of $T \lesssim 5\ \mu$K are expected [7,8,18,19]), studied for Rabi frequencies $\Omega \in 2\pi \times$ [100, 200] kHz [see Fig. 5(e)]. Intuitively, higher Ω_c is more forgiving of higher T, and we predict pulse fidelities exceeding 0.99 with $\Omega_c = 2\pi \times 200$ kHz for $T \lesssim 10\ \mu$K. Note that although we focus here on a single, relatively high trap frequency [8,9,13,17], the situation improves with lower ω_r, as shown nicely in Ref. [18]. Conceptually, a lower trap frequency gives slower atomic motion which decreases the Doppler shift. Figure 6 shows Rabi oscillations under the conditions indicated with shapes in Fig. 5. Indeed, we find the limit $\Omega_c \gg \omega_r$ to be relatively immune to thermal effects, as shown for $T = 20\ \mu$K in Fig. 6(d). Note that, depending on B, the π-pulse fidelity will begin to decrease with increasing Ω simply because of the increasing coupling to the "spectator" states. We study this interplay of Ω and B in Appendix I.

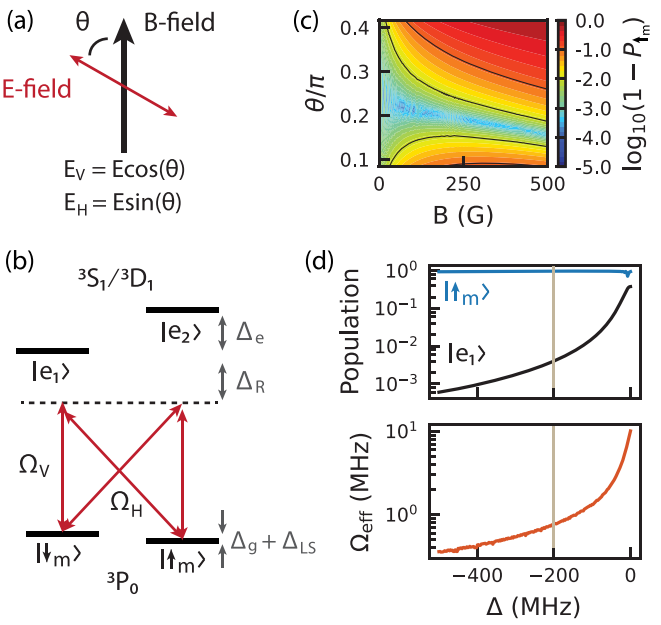

FIG. 7. Single-beam Raman gates. (a) The polarization axis (electric field) of the linearly polarized Raman beam with respect to the quantization axis (magnetic field), given by θ, determines the projections of the electric field onto the vertical and horizontal axes (parallel and perpendicular to the magnetic field, respectively). (b) The m qubit in the clock state is off resonantly coupled to an additional excited state ($^3S_1$ or $^3D_1$) via its $F = \frac{1}{2}$ level. The vertical and horizontal components of the electric field drive π and σ transitions with Rabi frequencies Ω_V and Ω_H, respectively (see Appendix D). (c) The π-pulse infidelity of the m qubit versus θ and magnetic field with constant drive strength of the Raman beam, detuned from $|e_1\rangle$ by $\Delta_R = 2\pi \times 200$ MHz. The "magic" region showing improved transfer depends on B and narrows for larger fields. The contour lines show the 10^{-1} and 10^{-2} infidelity levels. Spontaneous emission is not included. (d) Ω_{eff} and $P_{\uparrow_m}$ and P_{e_1} (populations in the target m state and intermediate state $|e_1\rangle$, respectively) after a π pulse versus Δ_R for constant intensity corresponding to $\Omega_V = 2\pi \times 20$ MHz when $\theta = 0$.

V. SINGLE-BEAM RAMAN GATES

We now turn to a discussion of rotations of the nuclear qubits (single-qubit gates) via stimulated Raman pulses. Inspired by recent work demonstrating Raman-based control of the g qubit [18], we focus on single-beam Raman gates. Crucially, the splitting of the nuclear qubits is much smaller, even in modest field ($\lesssim$ kHz/G), than the target effective Rabi frequency of $\Omega_{\mathrm{eff}} \approx 2\pi \times 1$ MHz [18,28,29]. Thus, a single beam with a linear polarization tilted by an angle θ with respect to the quantization axis (magnetic field) [see Fig. 7(a)] can provide components that drive both the π and σ transitions of the Raman coupling [18] [see Fig. 7(b)]. As shown in Fig. 1(a), the g and m qubits can be controlled identically, only via a different intermediate state. For clarity, and to match our proposed architecture shown in Fig. 1(b), we focus on the m qubit which can be controlled via the $^3D_1$ or $^3S_1$ state.

The analysis of the clock transition suggests that operation at a magnetic field of $\gtrsim$200 G is required for effective implementation of the *omg* architecture. This large field significantly affects the gate operation not because of the Zeeman

shift of m qubit itself, but because of the shift on the intermediate state which has electronic angular momentum (∼MHz/G). Crucially, the detuning from the intermediate state Δ_R is approximately equal to the Zeeman splitting on its sublevels Δ_e under the conditions considered here [see Fig. 7(b)]. Therefore, the use of a $F = \frac{3}{2}$ level for the intermediate state at high field would be drastically different than the low-field case studied recently where $\Delta_R \gg \Delta_e$ [18].

Instead, we consider a $F = \frac{1}{2}$ level, which is available for both $^3S_1$ and $^3D_1$. At a high field where $\Delta_R \approx \Delta_e$, the intermediate state coupling via $m_F = -\frac{1}{2}$ is significantly stronger than via $m_F = \frac{1}{2}$ for a red-detuned laser, which also means that $m_F = -\frac{1}{2}$ contributes more to the light shifts on the m qubit from the Raman pulse. This presents a unique opportunity: we predict a "magic" polarization angle $\theta = \theta_m(B)$ for which the differential light shift on the m qubit, Δ_{LS}, exactly cancels its Zeeman splitting Δ_g. Performing the Raman gates at this magic angle constitutes a pure σ_x rotation on the Bloch sphere, obviating complications due to the inevitable $\alpha\sigma_x + \beta\sigma_z$ nature of the rotation when Δ_g is left uncompensated. Figure 7(c) shows the π-pulse infidelity for the m qubit versus θ and the magnetic field, clearly showing excellent transfer in a region around $\theta_m(B)$ that narrows as B increases. These data use $\Delta_R = 2\pi \times 200$ kHz, and $\Omega_{\mathrm{eff}} \approx 2\pi \times 1$ MHz. Figure 7(d) shows Ω_{eff} and $P_{\uparrow_m}$ and P_{e_1} (populations in the target m state and intermediate state $|e_1\rangle$, respectively) after a π-pulse versus Δ_R for constant intensity corresponding to $\Omega_V = 2\pi \times 20$ MHz when $\theta = 0$ (see Appendix D). Technical challenges for targeted gates with a tightly focused beam are considered in Appendix J.

We focus on $\Delta_R = 2\pi \times 200$ kHz, which is used in Fig. 7(c). As shown in Fig. 7(d), the population in $|e_1\rangle$ is $P_{e_1} \approx 4 \times 10^{-3}$ under this value of Δ_R. Since the intermediate state has a total decay rate of $\Gamma_e \approx 2\pi \times 500$ kHz for $^3D_1$, the effective scattering rate from $|e_1\rangle$ is $\Gamma_e^{\mathrm{eff}} \lesssim 2\pi \times 2$ kHz, which we should compare to $\Omega_{\mathrm{eff}} \lesssim 2\pi \times 1$ MHz, suggesting that Raman π-pulse fidelities well above 0.99 are possible. Arbitrary rotations on the Bloch sphere can be accomplished by using additional pulses with $\theta = 0$ or $\pi/2$ such that there is no Raman condition and the pulse only provides a light shift for the $|\downarrow_m\rangle$ or $|\uparrow_m\rangle$ state, respectively, thereby providing a controlled σ_z rotation [18].

VI. CONCLUSION AND OUTLOOK

This analysis demonstrates that the structure of ^{171}Yb is well suited for high-fidelity quantum circuits featuring multiple-qubit modalities within the same atom. For concreteness, we focus on ground-clock and clock-Rydberg Rabi frequencies of $\Omega_c = 2\pi \times 200$ kHz and $\Omega_R = 2\pi \times 6$ MHz, respectively, and we show operation fidelities on both transitions exceeding 0.99 under magnetic fields of $B \gtrsim 200$ G and polarization impurities of $\chi \gtrsim 10^{-2}$. Additionally, we analyze temperature effects on the clock transition (and refer to Refs. [12,64] and Appendix K for consideration of such effects on the Rydberg transition), finding that $T \lesssim 10\ \mu$K is sufficient for clock pulses with fidelity exceeding 0.99. Finally, we analyze single-beam Raman gates for rotations of nuclear spin qubits and identify a "magic" linear polarization angle where the pulse-induced light shift perfectly cancels the nuclear Zeeman shift. We show the feasibility of purely σ_x rotations with $\Omega_{\mathrm{eff}} \approx 2\pi \times 1$ MHz at fidelities exceeding 0.99. All these conditions are readily available in current experiments.

We specifically considered ^{171}Yb to exploit its $I = \frac{1}{2}$, built-in nuclear spin qubits; however, other isotopes including ^{173}Yb and ^{87}Sr with larger I offer similar opportunities albeit with additional control fields required to isolate only two nuclear spin states [17]. Nevertheless, larger-I isotopes offer unique opportunities for SU(N) physics [34,67] and higher-dimensional computational spaces such as qudecimals [68] that could be leveraged for robust encoding [69]. In terms of the structure of S-series Rydberg states for isotopes with $I > \frac{1}{2}$, we expect a similar behavior where the $^3S_1$ $F_{\max} = 1 + I$ is well behaved since it is a unique configuration of electron and nuclear spins [51,53–55].

The *omg* architecture discussed in this work uniquely enables opportunities for shelving-based readout [7,17,42,43] as well as remote entanglement [37,38]. However, we note that other variants of this versatile *omg* architecture offer additional opportunities not discussed here. More generally, this platform holds promise for programmable entanglement in atomic clocks [39–41], quantum networking [37,38], and quantum computation [32–34,36]. A similar *omg* architecture has recently been proposed [28] and demonstrated [70] for trapped ions, where the additional required primitive operations are already compatible with existing large-scale systems. We believe the same is true for the neutral AEA-based platform [13–15,17–19].

Note added. Recently, we became aware of another work considering Rydberg-mediated gates for metastable $^3P_0$ nuclear spin qubits in ^{171}Yb [71].

ACKNOWLEDGMENTS

We thank B. Merriman, A. Desai, I. Madjarov, H. Bernien, A. Kaufman, and J. Thompson for helpful discussions. We acknowledge funding from the NSF QLCI for Hybrid Quantum Architectures and Networks (NSF Award No. 2016136), the NSF PHY Division (NSF Award No. 2112663), and the NSF Quantum Interconnects Challenge for Transformational Advances in Quantum Systems (NSF Award No. 2137642). C.H.G. is supported in part by the AFOSR-MURI, Grant No. FA9550-20-1-0323.

APPENDIX A: MULTICHANNEL QUANTUM DEFECT THEORY

Previous studies of neutral Yb Rydberg levels have determined a multichannel quantum defect theory (MQDT) representation of the energy-level spectrum, including perturbing levels of valence character (such as $6p^2$ or $4f^{13}5d^26p$). For the spin-0 isotopes of Yb, this provides a nearly complete characterization of many symmetries of the Rydberg series in the energy range extending to approximately 0.05 eV (12.1 THz) below the lowest ionization threshold. However, for a nuclear spin $I = \frac{1}{2}$ isotope such as ^{171}Yb, the hyperfine splitting can couple different J channels, and in particular the hyperfine interaction causes a strong coupling between the $6sns$ $^1S_0$ and

$6sns\ ^3S_1$ Rydberg series that gets very strong for Rydberg state binding energies that are comparable to the hyperfine splitting in the Yb^+ ion.

The basic theory that describes hyperfine-induced coupling of different electronic angular momentum channels in an atom follows the basic ideas of the frame transformation theory introduced into MQDT (FT-MQDT) by Fano, Lu, and Lee [58,72,73]. The theory was adapted to the specific context of hyperfine coupling by Sun and Lu [74,75] and extended to heavier complex atoms by Robicheaux *et al.* [53]. Our implementation of the theory in the present context focuses on the two channels that have singlet and triplet character mixed primarily by the hyperfine splitting of the $Yb^+(6s_{1/2})$ ionic core. We omit the closed subshell $4f^{14}$ from our notation except in contexts where its open-shell excitations arise. In FT-MQDT, the key quantity to determine is the reaction matrix $\underline{K}$, in an appropriate representation of the long-range channels.

For the $6sns$ Rydberg states of interest here, the only angular momentum quantum numbers are the ionic core spin $s_c = \frac{1}{2}$, the Rydberg electron spin $s = \frac{1}{2}$, and the nuclear spin $I = \frac{1}{2}$ for ^{171}Yb. The reaction matrix is first determined for each value $J = S$ of the electronic angular momentum, which is a good quantum number when neglecting the hyperfine interaction altogether. The singlet quantum defect μ_0 used here has been taken from Ref. [76], while the triplet μ_1 is taken from Ref. [10]. Specifically, the electronic reaction matrix is diagonal in the singlet-triplet representation, i.e., $K_{SS'} = \delta_{SS'} \tan \pi \mu_S$. Note that we have approximated the singlet and triplet quantum defects as energy independent, but this could easily be improved to obtain spectroscopic accuracy for these calculations. When the nuclear spin Hilbert space is included, this "eigenchannel representation" [56] of the reaction matrix for the quantum number $F = \frac{1}{2}$ characterizing the total angular momentum $\mathbf{F} = \mathbf{I} + \mathbf{S}$ has the structure

$$\langle [I(s_c s)S] F M_F | \underline{K} | [I(s_c s)S'] F M_F \rangle. \tag{A1}$$

The first step of the FT-MQDT is application of a straightforward recoupling into a representation that includes the total angular momentum quantum number of the core. That is needed because the ionization thresholds depend on the *ionic* core total angular momentum $f_c = 0$ or 1, where $f_c = \mathbf{I} + \mathbf{s}_c$. The recoupling coefficient looks like $\langle (I s_c) f_c | [I(s_c s)S] \rangle^{(F)}$, which is proportional to a $6j$ coefficient as in standard references. The resulting two-channel FT-MQDT K matrix which can be viewed as energy independent for sufficiently high Rydberg states with $n \gtrsim 35$ is equal to

$$\underline{K} = \begin{pmatrix} 4.1088 & 1.6922 \\ 1.6922 & 2.1549 \end{pmatrix}, \tag{A2}$$

where the first channel corresponds to the lower ionic hyperfine threshold $f_c = 0$ and the second channel corresponds to the upper threshold $f_c = 1$. If we set the zero of our energy scale to the degeneracy-weighted average of the two hyperfine thresholds, the two threshold energies E_{f_c} are given in terms of the hyperfine splitting $\Delta_{\rm HFS} = 2\pi \times 12.642\,812\,1$ GHz as $\{E_0/h = -9.482\,109,\ E_1/h = 3.160\,703\}$ GHz.

At this point, bound-state energies E_n are determined by solving for roots of the following equation:

$$\det \{\underline{K} + \tan \pi \underline{\nu}\} = 0, \tag{A3}$$

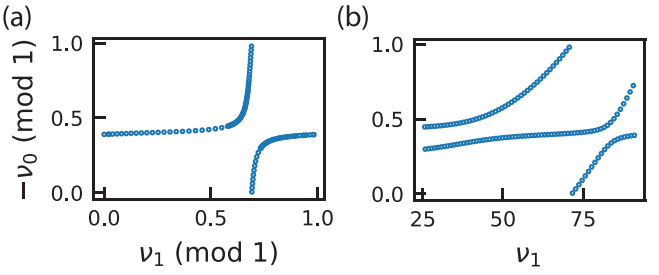

FIG. 8. Lu-Fano plots for the bound-state quantum defects of the two-channel $F = \frac{1}{2}$ series. Shown in (a) is the periodic version of the Lu-Fano plot [58], with the quantum defect relative to the lower ($f_c = 0$) hyperfine ionization threshold on the y axis, modulo 1, and the effective quantum number relative to the upper ($f_c = 1$) threshold on the x axis, also modulo 1. In the approximation used here, namely, with an energy-independent K matrix as is written above, the plot is exactly periodic. The extent of the channel coupling is reflected in the strength of the avoided crossing near the center of the figure. In (b) the plot shows the same bound levels, but without applying the (modulo 1) to the x axis effective quantum number data. The approximately horizontal branch is close to the $^3S_1$ quantum defect value, and from (b) it can be deduced that no significant level perturbations to that series should occur for ν_1 in the range 40 to 75.

where the diagonal matrix $\underline{\nu}$ consists of effective quantum numbers in the two channels, defined for energies below the lower threshold, by

$$\nu_{f_c}(E) = \sqrt{\frac{\mathrm{Ry}(^{171}\mathrm{Yb})}{E_{f_c} - E}}. \tag{A4}$$

Here, $\mathrm{Ry}(^{171}\mathrm{Yb})$ is the Rydberg constant for this electron-ion system, i.e., the infinite mass Rydberg constant multiplied by the ratio between the reduced electron-$^{171}Yb^+$ mass and the bare electron mass.

The resulting bound-state Rydberg energy levels are displayed in the form of Lu-Fano plots [58] in Fig. 8. These Lu-Fano plots illustrate the behavior of the $F = \frac{1}{2}$ Rydberg series as the principal quantum number increases. The energy levels with respect to the ground state are obtained by inverting (A4) to calculate E_{f_c}, and subsequently shifting them by the energy of the lower ionic hyperfine threshold relative to the ground state. These values are plotted in Fig. 2(d). We note that near degeneracies occur between the two series in the region where they begin to diverge and then slip by modulo 1 in Fig. 8. It is thus best to avoid this regime, which is why we focus on $n^* \approx 55$.

It should be noted that the present two-channel model of the $6sns$ Rydberg series does not include some of the channels that can cause additional perturbations, as have been studied in the literature. See Figs. 4 and 5 of Ref. [76], for example, which shows that level perturbations such as $4f^{14}6p^2$ and $4f^{13}5d6s6p$ occur for low principal quantum numbers below about $n \approx 25$, but these are unlikely to occur for any of the Rydberg series considered in this study. Strictly speaking, the $F = \frac{1}{2}$ Rydberg series and Lu-Fano plot should include the $6snd\ ^3D_1$ Rydberg series as well, but our estimates suggest that the amplitude of mixing with the $6sns\ ^3S_1$ series is small and only of order 10^{-3}, and for this reason the $6snd$ series are not included in our MQDT model. Moreover, the $^3D_1$

and $^3D_2$ quantum defects are in the range 0.72–0.76 and thus well separated from the $6sns$ levels of interest here. Similarly, an exact treatment of the $F = \frac{3}{2}$ series would include the coupling of $^3S_1$ states to $^1D_2$, $^3D_1$, and $^3D_2$ series, but those are also neglected here because the coupling is expected to be small for this total angular momentum as well.

APPENDIX B: THE $F = \frac{3}{2}$ $^3S_1$ RYDBERG SERIES

1. Bare energies relative to $F = \frac{1}{2}$

The $F = \frac{3}{2}$ $^3S_1$ Rydberg series is a simpler series to handle than the $F = \frac{1}{2}$ series due to the fact that it is a single channel converging to the $f_c = 1$ ionization threshold. In order to calculate the energy levels, however, we require the knowledge of the quantum defect of the $^3S_1$ Rydberg series. Due to a lack of experimental spectroscopic data for ^{171}Yb, we draw upon available data for the bosonic ^{174}Yb isotope to deduce the quantum defect. In particular, the $^3S_1$ series has been mapped out in Ref. [10]. The energy levels for the ^{171}Yb $F = \frac{3}{2}$ $^3S_1$ series are obtained by finding the effective quantum numbers from the measured levels and applying them in (A4). Note that we use the $f_c = 1$ ionization threshold. This shows that the $F = \frac{3}{2}$ and $\frac{1}{2}$ series are well separated by at least $\approx$10 GHz over the range of effective quantum number n^* shown in Fig. 2(d), eventually widening to the hyperfine splitting of the ionic core of $\Delta_{\mathrm{HFS}} = 2\pi \times 12.6$ GHz.

2. g factor of the $F = \frac{3}{2}$ series

Due to the simplicity of the single-channel nature of this series, the respective S_{tot}, J, and F angular momenta are well defined, with the caveats mentioned at the end of Appendix A. This permits the use of the standard result for calculating the g factor for this series at low magnetic fields. At low fields, the total angular momentum $\mathbf{F}$ precesses about the applied field. Thus, we aim to write

$$E_Z = -\langle \boldsymbol{\mu} \cdot \mathbf{B} \rangle = g_F m_F \mu_B B, \tag{B1}$$

where g_F is the g factor of interest.

The magnetic moment depends on the total spin of the electrons $\mathbf{S}$ and the nuclear spin $\mathbf{I}$. Since $\mathbf{F} = \mathbf{S} + \mathbf{I}$, we can project the respective angular momenta onto F to evaluate the matrix element:

$$\langle \mathbf{A} \rangle = \frac{\langle \mathbf{A} \cdot \mathbf{F} \rangle}{F(F+1)} \langle \mathbf{F} \rangle. \tag{B2}$$

The dot product can be evaluated easily as

$$\langle \mathbf{S} \cdot \mathbf{F} \rangle = \frac{\hbar m_F}{2F(F+1)} [F(F+1) + S(S+1) - I(I+1)], \tag{B3}$$

$$\langle \mathbf{I} \cdot \mathbf{F} \rangle = \frac{\hbar m_F}{2F(F+1)} [F(F+1) + I(I+1) - S(S+1)]. \tag{B4}$$

Packaging everything together gives

$$g_F = g_S \frac{F(F+1) + S(S+1) - I(I+1)}{2F(F+1)} - g_I \frac{\mu_N}{\mu_B} \frac{F(F+1) - S(S+1) + I(I+1)}{2F(F+1)}. \tag{B5}$$

With $g_S = 2$, $g_I = 0.4919$, $F = \frac{3}{2}$, $S = 1$, $I = \frac{1}{2}$, the g factor evaluates to 1.9 MHz/G.

3. Diamagnetic shift of the Rydberg series

As mentioned in the main text, the Rydberg states experience an additional diamagnetic shift in its energy due to a magnetic field. The diamagnetic Hamiltonian, given by

$$H_{\mathrm{DM}} = \frac{1}{8m_e} |\mathbf{d} \times \mathbf{B}|^2, \tag{B6}$$

arises from the term quadratic in the vector potential $\mathbf{A}$ in the Hamiltonian for a charged particle in an external electromagnetic field. This quadratic term is typically neglected in comparison to the linear term ($\mathbf{A} \cdot \mathbf{p}$), which is responsible for the linear Zeeman effect. However, due to the scaling of $\mathbf{d}$ as n^2 for Rydberg atoms, we anticipate that the quadratic term is comparable or even larger than the linear term. Thus, it is important to explicitly determine the energy shift due to the diamagnetic interaction.

To calculate the diamagnetic shift, it will be fruitful to expose the angular dependence of the Hamiltonian by writing it in terms of spherical harmonics $Y_{lm}(\theta, \phi)$. Since the cross product squared yields a factor of $\sin^2\theta = 1 - \cos^2\theta$, we can rewrite it as

$$\Delta E_{\mathrm{DM}} = \frac{e^2 B^2}{8m_e} \langle r^2 \sin^2\theta \rangle \tag{B7}$$

$$= \frac{e^2 B^2}{8m_e} \frac{4\sqrt{\pi}}{3} \left\langle r^2 \left(Y_{00} - \frac{1}{\sqrt{5}} Y_{20} \right) \right\rangle. \tag{B8}$$

An application of the Wigner-Eckart theorem reduces the problem to calculating the reduced matrix element of the r^2 operator and the factors arising from the angular dependence. The former can be dealt with using a variety of numerical tools developed in recent years to calculate matrix elements of Rydberg states. In particular, we utilize the ALKALINE RYDBERG CALCULATOR(ARC) 3.0 package [77] as the code has been expanded recently to support calculations for AEAs. For the angular-dependent factors, we find that for the $^3S_1$, $F = \frac{3}{2}$ manifold, only Y_{00} contributes a nonzero value. Moreover, it is independent of the m_F values. It follows that the four Zeeman states experience the same diamagnetic shift which scales as

$$\Delta E_{\mathrm{DM}}/h = 2.4\,\mathrm{kHz/G}^2. \tag{B9}$$

Comparing with the linear Zeeman shift of 1.9 MHz/G, we see that the two shifts become comparable at $\sim$800 G. Thus, we may neglect the diamagnetic shifts for most purposes. In any case, the diamagnetic shift does not affect the energy selectivity due to the equal shifts of all m_F states.

4. Hyperfine mixing between Rydberg series

We address the possibility of hyperfine mixing within the $^3S_1$ Ryberg manifold by diagonalizing the full Zeeman Hamiltonian for the Rydberg atom, treating the nucleus, the $6s$ core electron, and the Rydberg electron as separate entities. The basis of choice is the hyperfine basis $|[(Is_c)f_c s]FM_F\rangle$. We find that the Zeeman shift is linear for the $m_F = \pm\frac{1}{2}$ states in the two series, up to 1000 G, indicating that there is no significant mixing between the Rydberg series.

Another possible mixing channel is the diamagnetic coupling between the $^3S_1$ and ^3D_J manifolds. This arises from the Y_{20} term in the diamagnetic Hamiltonian. We assume that the coupling is significant when $|\langle ^3S_1|H_{\rm DM}|^3D_J\rangle|/|E(^3D_J) - E(^3S_1)| \gtrsim 0.1$, corresponding to ≈10% amplitude admixture. To get an order-of-magnitude estimate, we neglect the angular dependency in $\langle r^2 \sin^2\theta\rangle$ by taking $\langle r^2\rangle \sim 5n^4/2$, effectively setting an upper bound for the matrix element, and use $|E(^3D_J) - E(^3S_1)| \sim 0.3/n^3$ (atomic units). For $n^* \approx 55$, the 10% amplitude admixture occurs at $B \approx 600$ G, rendering this effect negligible at ≈200 G.

APPENDIX C: HYPERFINE MIXING IN THE "CLOCK" STATE

For the bosonic species of AEAs, the clock transition is typically doubly forbidden as it is a $J = 0$ to $J' = 0$ transition, with $\Delta S = 1$. On the other hand, the fermionic species has a weak admixture of the $^3P_0$ clock state with the $^1P_1$ state arising from the hyperfine mixing of states with the same F. This small $^1P_1$ character in the clock state enables a nonzero electric dipole coupling between the clock and ground states.

Although the hyperfine mixing allows us to drive the transition between the ground and clock states at large Rabi frequencies (∼200 kHz as stated in the main text), the hyperfine mixing complicates the Zeeman effect experienced by the clock hyperfine sublevels in the presence of a magnetic field. The full Zeeman effect is described by the total Hamiltonian

$$H_{\rm total} = H_Z + H_A + H_Q, \tag{C1}$$

where we have the usual Zeeman Hamiltonian

$$H_Z = -\boldsymbol{\mu}\cdot\mathbf{B}, \tag{C2}$$

and the corrections from the hyperfine and quadrupole effects

$$H_A + H_Q = A\mathbf{I}\cdot\mathbf{J} + Q\frac{\frac{3}{2}\mathbf{I}\cdot\mathbf{J}(2\mathbf{I}\cdot\mathbf{J}+1) - IJ(I+1)(J+1)}{2IJ(2I-1)(2J-1)}. \tag{C3}$$

We will need to diagonalize (C1) in order to describe the Zeeman effect across all values of the applied magnetic field. We adopt the methods and convention of [21] to calculate the Zeeman map of the clock state across a large range of magnetic field values. Accordingly, the Zeeman Hamiltonian of (C2) is written as

$$H_Z = (g_s S_z + g_l L_z - g_I I_z)\mu_0 B, \tag{C4}$$

where $g_s \approx 2$, $g_l = 1$, $g_I = \frac{\mu_I}{\mu_B|I|}$ are the g factors of the electron spin, orbital angular momentum, and nuclear spin, respectively; and $\mu_0 = \mu_B/h$ is the Bohr magneton in units of Hz/T. The angular momentum operators here are dimensionless. The quadrupole Hamiltonian can be dropped as $Q = 0$ for $I = \frac{1}{2}$ [57]. Thus, the only correction that we need to include is H_A.

For the $^1S_0$ ground state, it experiences only a linear Zeeman shift due to the fact that $\mathbf{J} = 0$, hence, there is no hyperfine correction. Thus, the energy shift (in units of Hz) is

$$\Delta\nu(^1S_0, m_F) = -g_I m_F \mu_0 B. \tag{C5}$$

TABLE I. Table of parameters for ^{171}Yb. Parameters with † are taken from [78].

Parameter	Value
$\lvert\alpha\rvert^\dagger$	0.996
$\lvert\beta\rvert^\dagger$	0.125
$\delta g^\dagger$	2.73×10^{-4}
$\lvert\alpha_0\rvert$	1.41×10^{-4}
$\lvert\beta_0\rvert$	3.33×10^{-5}

For the $^3P_0$ clock state, the hyperfine mixing between the $^3P_0$ and $^3P_1$ states leads to a Breit-Rabi expression given by

$$\nu(^3P_0, m_F) = \frac{1}{2}[\nu(^3P_0) + \nu(^3P_1)] + \frac{1}{2}[\nu(^3P_0) - \nu(^3P_1)] \times \sqrt{1 + 4\frac{\sum_{F'}\alpha^2\left|\langle ^3P_0^0, F|H_Z|^3P_1, F'\rangle\right|^2}{[\nu(^3P_0) - \nu(^3P_1)]^2}}, \tag{C6}$$

where

$$\nu(^3P_0) = \nu(^3P_0^0) + \langle ^3P_0^0|H_Z|^3P_0^0\rangle + 2(\alpha_0\alpha - \beta_0\beta)\langle ^3P_1^0, F = I|H_Z|^3P_0^0\rangle, \tag{C7}$$

$$\nu(^3P_1) = \nu(^3P_1^0) + \sum_{F'}\left(\alpha^2\langle ^3P_1^0, F'|H_Z|^3P_1^0, F'\rangle + \beta^2\langle ^1P_1^0, F'|H_Z|^1P_1^0, F'\rangle\right). \tag{C8}$$

The matrix elements are taken between states of pure LS nature, as denoted by the superscript 0. The constants $\{\alpha, \beta\}$ and $\{\alpha_0, \beta_0\}$ are known as the intermediate coupling and hyperfine mixing coefficients as they characterize the extent of the admixture of the atomic states:

$$|^3P_0\rangle = |^3P_0^0\rangle, \tag{C9}$$

$$|^3P_1\rangle = \alpha|^3P_1^0\rangle + \beta|^1P_1^0\rangle, \tag{C10}$$

and

$$|^3P_0, I, F\rangle = |^3P_0^0\rangle + (\alpha_0\alpha - \beta_0\beta)|^3P_1^0\rangle + (\alpha_0\beta + \beta_0\alpha)|^1P_1^0\rangle. \tag{C11}$$

Most importantly, these coefficients are related to experimentally measurable quantities:

$$\tau(^3P_1) = \left(\frac{\nu(^1P_1)}{\nu(^3P_1)}\right)^3\frac{\alpha^2}{\beta^2}\tau(^1P1); \tag{C12}$$

$$\tau(^3P_0) = \left(\frac{\nu(^3P_1)}{\nu(^3P_0)}\right)^3\frac{\beta^2}{(\alpha_0\beta + \beta_0\alpha)^2}\tau(^3P_1); \tag{C13}$$

$$\delta g = (\alpha_0\alpha - \beta_0\beta)\sqrt{\frac{8}{3I(I+1)}}, \tag{C14}$$

where τ is the lifetime of the state, and δg is the differential g factor for the clock state, such that $g_I(^3P_0) = g_I + \delta g$ at weak magnetic fields. These expressions can be used to estimate the values of the coupling constants, which are summarized in Table I.

APPENDIX D: NUMERICAL SIMULATION OF MULTILEVEL DYNAMICS

1. Method overview

We employ a numerical model to analyze the dynamics of the clock and Rydberg multilevel systems. For a general system of n states composing the basis $S = \{|1\rangle, \ldots, |n\rangle\}$ with energies $\hbar \times \{\omega_1, \ldots, \omega_n\}$, we write the total, time-dependent state $|\psi(t)\rangle$ as

$$|\psi(t)\rangle = \sum_{k=1}^{n} a_k(t) e^{-i\omega_k t} |k\rangle, \tag{D1}$$

where its "free-evolving" components have been explicitly divided out from the amplitudes $a_1, \ldots, a_n$. This choice is convenient for the later computation of phases discussed in Appendix D 3. In this frame, the Hamiltonian for the system in the presence of a drive of strength Ω and frequency ω has only off-diagonal components,

$$\hat{H}(t) = \hbar \sum_{b=1}^{n} \sum_{a<b} \frac{\Omega}{2} g_a^b(\chi, q) e^{i(\omega - \omega_0 - \widetilde{\omega}_a^b)t} |b\rangle\langle a| + \text{H.c.}, \tag{D2}$$

where the usual rotating-wave approximation comparing ω to some chosen reference energy ω_0 (e.g., the difference in mean energies of the ground and clock or clock and Rydberg manifolds) has been used, and $\widetilde{\omega}_a^b$ is the energy of the $a \leftrightarrow b$ transition relative to it. We also consider a transition-dependent factor $g_a^b(\chi, q)$ modulating the "principal" drive strength Ω of the targeted transition. $g_a^b(\chi, q)$ provides the correct couplings for specific polarizations $q \in \{0, \pm 1\}$ of the drive field, with additional weighting for impurities χ therein as well as Clebsch-Gordan coefficients, as discussed in the main text. In general, Ω and ω may be time dependent as well to account for intensity and/or phase noise, respectively (see Appendix F), in which case we take $\omega t \to \phi(t) = \int_0^t \omega(t')\, dt'$.

Expanding further on the transition-dependent drive strength modulation factor $g_a^b(\chi, q)$, we formally define this quantity in terms of two distinct parts

$$g_a^b(\chi, q) = \rho\left(\chi; m_F^a, m_F^b, q\right) \times W\left(F^a, m_F^a, F^b, m_F^b, q\right). \tag{D3}$$

The first, $\rho(\chi; m_F^a, m_F^b, q)$, accounts for effects due to polarization impurity in terms of the parameter χ introduced in the main text. With q held fixed for a given drive polarization, the corresponding weighting factor is $\sqrt{1-\chi}$ for transitions satisfying $m_F^b - m_F^a = q$, while for all other, "parasitic" transitions, the factor is $\sqrt{\chi/2}$ to conserve total power in the drive across all three possible polarizations:

$$\rho\left(\chi; m_F^a, m_F^b, q\right) = \begin{cases} \sqrt{1-\chi} & \text{if } m_F^b - m_F^a = q, \\ \sqrt{\chi/2} & \text{otherwise.} \end{cases} \tag{D4}$$

The second, $W(F^a, m_F^a, F^b, m_F^b, q)$, imposes weighting by Clebsch-Gordan coefficients and dipole selection rules on all nonprincipal transitions, normalized to that for the targeted transition. This factor is conveniently defined in terms of the usual Wigner $3j$ symbols,

$$W\left(F^a, m_F^a, F^b, m_F^b, q\right) = \frac{\begin{pmatrix} F^b & 1 & F^a \\ m_F^b & m_F^a - m_F^b & -m_F^a \end{pmatrix}}{\begin{pmatrix} F^b & 1 & F^a \\ \bar{m}_F^b & -q & -\bar{m}_F^a \end{pmatrix}}, \tag{D5}$$

where $\bar{m}_F^a$ and $\bar{m}_F^b = \bar{m}_F^a + q$ are the quantum numbers of the principal transition. The values of this function used for our calculations are shown in Table II.

TABLE II. Table of Clebsch-Gordan weighting factors for all transitions of interest in this work in the presence of a σ^+ ($q = 1$) drive, according to Eq. (D5).

F^a	m_F^a	F^b	m_F^b	$W(F^a, m_F^a, F^b, m_F^b, 1)$
		Ground-clock ($^1S_0 \leftrightarrow {}^3P_0$)		
1/2	+1/2	1/2	+1/2	$\sqrt{1/2}$
	+1/2		−1/2	1
	−1/2		+1/2	1
	−1/2		−1/2	$\sqrt{1/2}$
		Clock-Rydberg ($^3P_0 \leftrightarrow {}^3S_1$)		
1/2	+1/2	3/2	+3/2	1
	+1/2		+1/2	$\sqrt{2/3}$
	+1/2		−1/2	$\sqrt{1/3}$
	−1/2		+1/2	$\sqrt{1/3}$
	−1/2		−1/2	$\sqrt{2/3}$
	−1/2		−3/2	1

With these definitions, we include as an example the form of the Hamiltonian for the six-level clock-Rydberg manifold, subject to a σ^+ drive on resonance with the $|\uparrow_m\rangle \leftrightarrow |r\rangle$ transition:

$$\hat{H}_{c\leftrightarrow R} = \hbar\frac{\Omega}{2}\begin{bmatrix} 0 & 0 & \text{H.c.} & \text{H.c.} & \text{H.c.} & 0 \\ 0 & 0 & 0 & \text{H.c.} & \text{H.c.} & \text{H.c.} \\ \sqrt{\frac{\chi}{2}} w\left(-\frac{1}{2}, -\frac{3}{2}\right) e^{i(3\Delta+\delta)t} & 0 & 0 & 0 & 0 & 0 \\ \sqrt{\frac{\chi}{2}} w\left(-\frac{1}{2}, -\frac{1}{2}\right) e^{i(2\Delta+\delta)t} & \sqrt{\frac{\chi}{2}} w\left(+\frac{1}{2}, -\frac{1}{2}\right) e^{i2\Delta t} & 0 & 0 & 0 & 0 \\ \sqrt{1-\chi}\, w\left(-\frac{1}{2}, +\frac{1}{2}\right) e^{i(\Delta+\delta)t} & \sqrt{\frac{\chi}{2}} w\left(+\frac{1}{2}, +\frac{1}{2}\right) e^{i\Delta t} & 0 & 0 & 0 & 0 \\ 0 & \sqrt{1-\chi} & 0 & 0 & 0 & 0 \end{bmatrix} \begin{matrix} |\downarrow_m\rangle \\ |\uparrow_m\rangle \\ |r_{\Downarrow}\rangle \\ |r_{\downarrow}\rangle \\ |r_{\uparrow}\rangle \\ |r\rangle \end{matrix}. \tag{D6}$$

Here, we write the six-state basis for the clock-Rydberg manifold as $\{|\downarrow_m\rangle, |\uparrow_m\rangle, |r_{\Downarrow}\rangle, |r_{\downarrow}\rangle, |r_{\uparrow}\rangle, |r\rangle\}$, where the Rydberg states $|r_X\rangle$ are ordered by their m_F values. For brevity, we also use $w(m_F^a, m_F^b) \equiv W(\frac{1}{2}, m_F^a, \frac{3}{2}, m_F^b)$ and define Δ and δ as the

differences in energy (up to a factor of $\hbar$) between the adjacent m_F states in the Rydberg and clock manifolds, respectively.

For the multiatom case of the clock-Rydberg transition, we generate the appropriate Hamiltonian for N atoms in the product-state basis $\mathbb{S} = S^N$ using the single-atom form in Eq. (D2):

$$\hat{\mathbb{H}}_N(t) = \sum_{k=1}^{N} \hat{\mathbb{I}}^{\otimes k-1} \otimes \hat{H}_k \otimes \hat{\mathbb{I}}^{\otimes N-k} + \sum_{|A\rangle,|B\rangle\in\mathbb{S}} V_{A,B}|A\rangle\langle B|, \tag{D7}$$

where $\hat{\mathbb{I}}$ is the $n \times n$ identity operator for a single atom, $\hat{H}_k$ is the single-atom Hamiltonian for the kth constituent, and $\otimes$ denotes the Kronecker product. $V_{A,B}$ encodes interactions at the atom-atom level between the N-atom states $|A\rangle$ and $|B\rangle$ including, for instance, the U_{VdW} Rydberg interaction.

Numerical simulation is accomplished using the standard fourth-order Runge-Kutta integration scheme [79] for the Schrödinger equation. We define the grid of discretized times $t^k = k\,dt\,,\ \ k = 0, \ldots, N_t$ over which the state vector is integrated using the time-discretized Hamiltonian $\hat{H}^k = \hat{H}(t^k)$ for $dt \ll 2\pi/\Omega$ suitably short and $N_t\,dt$ appropriately long.

2. Magnetic field noise

We are additionally interested in analyzing the effect of magnetic field noise on the atomic dynamics. We first note that fluctuations should occur over timescales corresponding to $\lesssim$ kHz frequencies due to large inductances expected in coils found in realistic experimental apparatuses. Thus, we can assume that the field noise is slow compared to our laser pulses, and hence we consider a field that varies only on a shot-to-shot basis. To simulate this, we average the time evolution of the state vector over a series of N trials (we use $N = 30$ in our calculations), for each of which the magnetic field strength B is sampled from a Gaussian distribution with standard deviation 1 mG and variable mean value held fixed for all trials. We choose the standard deviation as a good approximation to the Johnson white noise found in servos that are typically used to control the current in magnetic coils [59,60].

We consider magnetic field noise in this way for the analyses of both the ground-clock and clock-Rydberg dynamics. We find that in both cases the effect of this noise is negligible, and in the latter it is indiscernible. We therefore only include it in this work for the ground-clock dynamics. The main effect of this noise, as stated in the main text, is to reduce the coherence time of the nuclear spin qubits to $T_2^* \gtrsim 1$ s. However, this effect can be mitigated by, e.g., dynamical decoupling.

3. Relative phase accrual on a qubit

Since we calculate the full evolution of the state vector, the integration scheme described above may also be used to find the relative phase accrued between two basis states over some time interval. Given the calculated time-dependent state vector $|\psi^k\rangle = |\psi(t^k)\rangle$, it is straightforward to find the relative phase between two components $|a\rangle$ and $|b\rangle$ of $|\psi^k\rangle$ as

$$\Delta\varphi_{a,b}^k = \arg\left(\frac{\langle a|\psi^k\rangle}{\langle b|\psi^k\rangle}\right). \tag{D8}$$

We note here that, recalling Eq. (D1), the free-evolving components of the phase have already been explicitly removed, and hence Eq. (D8) gives the accrued phase due only to externally applied drives to the dynamics.

For use in our numerical analysis of both the clock and Rydberg transitions, we are interested in calculating this relative phase between the two m_F states of the ground- (clock-) state manifold after an effective 2π pulse has been applied on the ground-clock (clock-Rydberg) transition. While the dynamics governing the value of this phase are in general complicated for the systems featured in this work, it is useful to consider the limit of strong magnetic field and small polarization impurity. In this limit, there are essentially no undesirable couplings, and hence both transitions simplify to a two-level system (states $|g\rangle$, $|e\rangle$ representing one state of a qubit and its corresponding excited state) undergoing Rabi oscillations with dressing from a third, uncoupled spectator state $|s\rangle$ (representing the other state of the qubit). We model the time dependence of the total state as

$$|\zeta(t)\rangle = \cos\left(\frac{\theta_0}{2}\right)\left[\cos\left(\frac{\Omega}{2}t\right)|g\rangle + \sin\left(\frac{\Omega}{2}t\right)e^{i\gamma(t)}|e\rangle\right] + \sin\left(\frac{\theta_0}{2}\right)e^{i\varphi_0}|s\rangle, \tag{D9}$$

where Ω is the Rabi frequency (defined in terms of oscillations in probability, not amplitude), and $\gamma(t)$ depends on the polarization and detuning of the drive. The constants θ_0 and φ_0 describe the initial state dressing, and we note that it is necessary to have $0 < \theta_0 < \pi$ (i.e., to have nonzero initial population in both $|g\rangle$ and $|s\rangle$) in order for the desired relative phase to be well defined. For the targeted case of a resonant drive in this work, we also take $\gamma(t) = 0$. From this, it is easily seen that at the targeted 2π time $\tau_{2\pi} = 2\pi/\Omega$, the relative phase accrued between the ground and spectator states over the duration of the drive is invariably π for all θ_0, φ_0:

$$|\zeta(\tau_{2\pi})\rangle = -\left[\cos\left(\frac{\theta_0}{2}\right)|g\rangle + \sin\left(\frac{\theta_0}{2}\right)e^{i(\varphi_0+\pi)}|s\rangle\right]. \tag{D10}$$

We note that, as seen in Figs. 3 and 5, the numerical calculations agree well with this expected behavior.

4. Modeling the single-beam Raman transitions

In order to show the existence of the "magic angle" for the single-beam Raman transitions between adjacent "m"-qubit states as in Fig. 7, we now move to a model featuring an atom in the presence of a driving field that has well-defined polarization. In this model, we consider a linearly polarized plane wave incident on an atom with k vector perpendicular to a surrounding magnetic field. Rather than its impurity χ, we parametrize the wave's polarization by θ, the angle between the electric and magnetic fields. Computationally, this amounts to replacing the weighting factor ρ defined in Eq. (D4) with another formulation $\widetilde{\rho}$ to be derived below.

We consider a cylindrically symmetric system (spanned by orthogonal unit vectors $\hat{r}$, $\hat{\varphi}$, and $\hat{z}$ in the typical fashion) with magnetic field oriented along the z axis. The incident plane wave is then defined to have k vector pointed along $\hat{r}$ and

polarization vector

$$\hat{\varepsilon}(\theta) = \hat{\varphi}\,\sin\theta + \hat{z}\,\cos\theta. \tag{D11}$$

Next, we define an additional set of orthogonal unit vectors $\hat{\epsilon}_q$ to describe the space of possible ways that a classical dipole moment may rotate,

$$\hat{\epsilon}_{\pm1} = \frac{1}{\sqrt{2}}(\hat{\varphi} \pm i\hat{r}), \quad \hat{\epsilon}_0 = \hat{z}, \tag{D12}$$

where the first two correspond to right-hand (parallel to $\hat{z}$) and left-hand (antiparallel to $\hat{z}$) rotation about the z axis, associated with $\sigma^{\pm}$ transitions, and the last to simple oscillation on the axis, associated with the π transition. Without loss of generality we may associate $\hat{\epsilon}_{+1}$ with the σ^+ transition specifically, and find the appropriate form for $\widetilde{\rho}$ as

$$\widetilde{\rho}\left(\theta; m_F^a, m_F^b\right) = \hat{\epsilon}^*_{m_F^b - m_F^a} \cdot \hat{\varepsilon}(\theta) \tag{D13}$$

$$= \begin{cases} \frac{1}{\sqrt{2}}\sin\theta & \text{if } \left|m_F^b - m_F^a\right| = 1, \\ \cos\theta & \text{if } m_F^b - m_F^a = 0. \end{cases} \tag{D14}$$

This modified polarization weight $\widetilde{\rho}$ is then inserted into Eq. (D3), replacing each instance of ρ.

To produce the results shown in Figs. 7(c) and 7(d), we consider driving the Raman transition specifically between the two m qubits, using the $^3D_1$ $F = \frac{1}{2}$, $m_F = -\frac{1}{2}$ state as the intermediary, although this system is easily mapped to cases where the use of a $^3S_1$ intermediary may be desirable, or when driving the "g" qubits (for equivalent F and m_F quantum numbers of the intermediary state), as shown in Fig. 1(a). In our simulations, we use a drive strength corresponding to $\Omega_V = 2\pi \times 20$ MHz when the angle θ between the driving electric and surrounding magnetic fields is zero. Estimating the reduced dipole matrix element for the $^3P_0 \leftrightarrow {}^3D_1$ transition from a mixture of past determinations [80], said drive strength requires approximately 2 mW of power in a beam of 1 mm waist radius. Of course, the required power will be much lower for targeted Raman gates with a tightly focused beam.

The subsequent analysis of the simulated dynamics of this system is identical to that for the clock and Rydberg transitions above: we evolve the system initialized to the $|{\downarrow_m}\rangle$ clock state using a Hamiltonian of the form given by Eq. (D2) and calculate π-pulse fidelity based on the resulting Rabi oscillations of the target $|{\uparrow_m}\rangle$ state, with the exception that here the effective Rabi frequency Ω_{eff} is also computed. Due to programmatic considerations, this is done in two ways. Specifically, we find that conditions corresponding to large regions of the considered parameter space give dynamics featuring high-frequency probability oscillations of sufficient amplitude as to make the determination of the effective 2π time (and by extension the effective Rabi frequency) difficult using only the time-domain oscillations. To combat this effect, we compute Ω_{eff} by two methods: The first-maximum (FM) method is to simply find the time corresponding to the first local maximum in the probability oscillations of the initial state and invert it to find the corresponding frequency. The second method (FT) is to find the frequency as the lowest-frequency component of the Fourier transform of either the target or initial states. The FM method is cheap to compute with good precision, but strongly affected by the aforementioned problem with high-frequency oscillations. On the other hand, the FT method escapes this problem, but requires one to simulate the dynamics out to longer times in order to give good resolution at low frequencies. For each set of conditions, Ω_{eff} is obtained via both methods; if the two results agree to within 5% of the FT value, then the FM result is preferred, otherwise the FT. We find that simulating to 25 μs gives good low-frequency resolution under the range of conditions considered.

APPENDIX E: OFF-RESONANT LIGHT SHIFTS AND SCATTER FROM CLOCK PULSES AND TWEEZERS

Beyond magnetic field stability, another important consideration for the fundamental limitation on coherent evolution is off-resonant dressing and scattering of the atoms from both the optical pulses and the tweezers. We focus on the clock pulse in particular since the proposed use case is unique, while this effect from the Rydberg pulse is universal and similar to other recent work [12,19].

When an atom is placed into a laser beam, the electrical field $\mathbf{E}$ causes the atomic dipole moment $\mathbf{p}$ to oscillate at the driving frequency according to $\mathbf{p} = \alpha\mathbf{E}$, where α is defined as the polarizability of the atom. The real part of the polarizability introduces the light shift and the imaginary part gives the scattering of the photons. The calculation of the atom's polarizability gives us the evaluation of both the light shift and scattering rate, which we consider for both the clock pulse and tweezers.

As we discussed previously, a Rabi frequency $\Omega_c = 2\pi \times 200$ kHz for the clock transition is a realistic value with reasonable polarization purity, temperature and magnetic field stability requirement. On the other hand, as we increase the Rabi frequency it is also accompanied with the sharp increasing of the clock pulse intensity due to the relation $\Omega_c \propto \sqrt{P_c}$, where P_c is power of the clock laser. Since the light shift is proportional to the intensity, the increasing of the Rabi frequency will also introduce a significant differential light shift between the ground and clock states that comes from the off-resonant coupling of the clock laser to all the other transitions. For the tweezers, this differential light shift is fully canceled under the given clock-magic wavelength [22].

In Fig. 9(a), we calculate both the Rabi frequency and the differential light shift introduced by the clock laser under various laser power for an assumed beam waist radius of $w = 20$ μm. (We focus on global pulses here, but will return to tightly focused pulses in Appendix J.) This suggests the off-resonant light shift is comparable to the Rabi frequency under our typical experiment condition, and thus laser intensity noise can be converted into a noticeable noise of laser detuning Δ. To evaluate the effect of this power fluctuation, we consider a simple two-level system, where a π pulse of $\Omega_c = 2\pi \times 200$ kHz indicates a square pulse length of $\tau = 2.5$ μs, which corresponds to a window function $W(\delta) = [\sin(\delta\tau/2)/(\delta\tau/2)]^2$ that filters out all the noise with a frequency significant higher than $1/\tau$, where δ is the frequency of the noise. Within this noise bandwidth, a stability better than 1% is trivial for an active power stabilization setup.

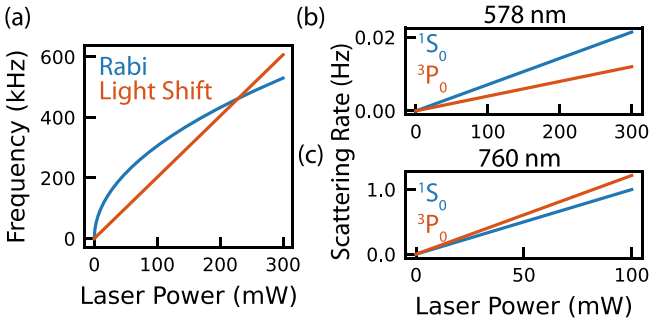

FIG. 9. Off-resonant light shifts and scatter from clock pulses and tweezers. (a) The Rabi frequency Ω_c and off-resonant differential light shift of the clock transition versus the clock laser power for a global readout beam (20 μm beam waist). (b), (c) The off-resonant scattering rate of ground ($^1S_0$) and metastable ($^3P_0$) states versus the clock laser power (b) and tweezer power (c).

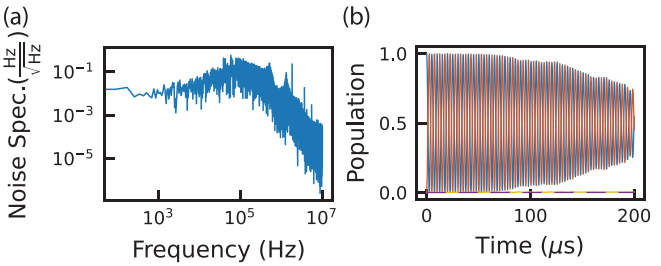

FIG. 10. Phase-noise effects from the clock laser. (a) Measured frequency noise spectrum from our cavity reflection without correcting for cavity rolloff. This is an approximation of the transmitted signal through the cavity that filters phase noise above the cavity bandwidth (≈5 kHz). (b) We simulate the ground-clock manifold in the presence of a drive with a time-dependent frequency as described in Sec. IV and Appendix D. This drive is measured data, which was used to generate the noise spectrum in (a). We find that high-contrast oscillations can be sustained for $\gtrsim$20 cycles before dephasing causes decay.

For the atom's transition under this effective frequency noise, a shot-to-shot population fluctuation of the excited state is $(\Delta/\Omega_c)^2 < (0.01)^2$ where the differential off-resonant light shift is significantly smaller than the Rabi frequency. Thus, the effect of this differential off-resonant light shifts is negligible under our usual conditions, but would become significant as $\Omega_c/2\pi$ approaches the MHz scale. On the other hand, a laser pointing error of 1.4 μm will also cause a 1% change of a laser intensity for a beam waist around 20 μm. This pointing error noise can either be removed by the occasionally checking the Rabi frequency during the experiment or by adding the active position feedback to the mirrors.

Beyond the effect of the differential light shift, the lifetime and the coherent time of the atom will be limited by the off-resonance scattering from both the clock pulse and tweezers. Figure 9(b) shows the calculation of the scattering rate on the relevant states of the atoms. The upper plot shows the calculated scattering rate from the clock laser to the ground and clock states. Under typical clock pulse intensity, we can find this off-resonance scattering rate is negligible compared to the Ω_c. Figure 9(c) gives the scattering rate of the tweezers at the clock-magic wavelength, which indicates a more than 1-s lifetime for both the ground- and metastable-state atoms under the typical power of the tweezers. This off-resonance scattering is also negligible for a 2.5-μs clock pulse, and we again emphasize that clock pulses are the slowest operation in our proposed architecture.

APPENDIX F: PHASE-NOISE ANALYSIS

Here we are interested in the dephasing effect of laser phase noise on Rabi oscillations [64] occurring within the ground-clock manifold. To analyze this effect under realistic conditions and demonstrate the robustness of our scheme, we characterize the phase noise from one of our own lasers, tuned to the $|{\downarrow_g}\rangle \leftrightarrow |{\uparrow_m}\rangle$ clock transition discussed in the main text, and use the measured data in a simulated drive of the four-state ground-clock manifold following the procedure described in Appendix D.

First, we describe the procedure to characterize the phase noise in the laser. Our "clock" laser ($\lambda = 578$ nm) is generated from the second harmonic of an infrared "master" laser at $\lambda_{\text{IR}} = 1156$ nm, which is locked via the Pound-Drever-Hall (PDH) technique to an ultrastable cavity system produced by Stable Laser Systems. We then use the slope of the in-loop PDH error signal from light reflected from the cavity to obtain the locked laser's frequency as a function of time and hence compute Allan deviation and the power spectral density (PSD) of this signal. The measured cavity response is limited by its linewidth $\nu_c \approx 5$ kHz, which gives significant attenuation of the signal near the frequency band of interest at ≈100 kHz. We could correct for this effect by including a "cavity rolloff factor" [81] to accurately portray the phase noise on our laser, but in this work we consider using the transmitted light through the cavity to filter this phase noise [62]. Hence, the phase noise of the transmitted light is accurately represented by our measurement of the reflected light directly, without including the cavity rolloff factor. We believe this approach will make our analysis more generally applicable. With this procedure we calculate the Allan deviation of the measured signal to be $\sigma \lesssim 2 \times 10^{-15}$ at a $\tau = 1$ s averaging time and estimate the linewidth of the laser to be $\Delta\nu \approx 2$ Hz from the PSD, shown in Fig. 10(a), using the β-separation line method [82].

The phase-noise data were then used to generate a realistic, time-dependent drive to a simulated four-level ground-clock manifold. This is accomplished by taking a sum over Fourier components that are weighted by the calculated PSD with random phase shifts sampled from a uniform distribution. When applied in simulation following the description given in Appendix D, we find that high-contrast Rabi oscillations can be sustained over more than 20 cycles with this drive, as shown in Fig. 10(b).

APPENDIX G: FINITE-TEMPERATURE MODELING

We now incorporate finite-temperature effects in our analysis of single-atom dynamics. In an optical tweezer, a single atom at nonzero temperature is delocalized over lengths comparable to the wavelength of the laser; hence, we must include

a position-dependent motional phase factor $\exp(i\mathbf{k}\cdot\mathbf{x})$ into the drive Ω, where $\mathbf{k}$ is the wave vector of the driving laser. $\eta = kx_0$ is the Lamb-Dicke parameter (see the main text). For simplicity, we approximate the tweezer with a one-dimensional harmonic trapping potential [18,66] and write the motional phase factor as $\exp[i\eta(\hat{a}+\hat{a}^\dagger)]$, where $\hat{a}$ and $\hat{a}^\dagger$ are ladder operators operating on the Fock basis $\{|n\rangle\}$ corresponding to the usual harmonic oscillator states. For brevity, we denote the motional phase factor and its adjoint as $\hat{\xi} = \exp[i\eta(\hat{a}+\hat{a}^\dagger)]$ and $\hat{\xi}^\dagger = \exp[-i\eta(\hat{a}+\hat{a}^\dagger)]$. For the case of a "magic" wavelength trap (where the atomic ground and excited states experience the same trap frequency), the Hamiltonian of the system is [18,66]

$$\hat{H} = \hbar\sum_{g,e}\frac{\Omega}{2}\left(g_g^e(\chi,q)e^{i(\omega-\omega_0-\tilde{\omega}_g^e)}\hat{\xi}\otimes|e\rangle\langle g| + \text{H.c.}\right) + \hbar\omega_t\left(\hat{a}^\dagger\hat{a}+\frac{1}{2}\right)\otimes\hat{\mathbb{I}}, \tag{G1}$$

where $|g\rangle \in \{|\downarrow_g\rangle, |\uparrow_g\rangle\}$ and $|e\rangle \in \{|\downarrow_m\rangle, |\uparrow_m\rangle\}$. $\hat{\mathbb{I}}$ is the 4×4 identity operator for the four-level ground-clock manifold. $\Omega g_g^e(\chi,q)$ is the driving term which includes both the effects of polarization impurity and Clebsch-Gordan weighting factor (see Appendix D).

For our purposes, we consider $\Omega \gg \omega_r$ for a high-fidelity state transfer. The higher-order terms of $\hat{\xi}$ are also no longer strongly suppressed and couple a single motional state to many other excited motional states at the same time. To simplify calculations we rewrite the basis states of the combined atom Fock Hilbert space as $|g,n\rangle = |g\rangle\otimes|n\rangle$ and $|e,\xi(n)\rangle = |e\rangle\otimes\hat{\xi}|n\rangle$. We then rewrite the Hamiltonian by inserting the identity resolved in this basis to the left and right,

$$\hat{H} \to \left(\sum_{n',g',e'}|g',n'\rangle\langle g',n'| + |e',\xi(n')\rangle\langle e',\xi(n')|\right)\hat{H} \times\left(\sum_{n,g,e}|g,n\rangle\langle g,n| + |e,\xi(n)\rangle\langle e,\xi(n)|\right), \tag{G2}$$

and define a four-level state vector G_n for the nth motional state

$$G_n = (|\uparrow_m,\xi(n)\rangle, |\downarrow_m,\xi(n)\rangle, |\uparrow_g,n\rangle, |\downarrow_g,n\rangle). \tag{G3}$$

Thus, the Hamiltonian can be simplified as

$$\hat{H} \to \left(\sum_{n'}G_{n'}G_{n'}^\dagger\right)\hat{H}\left(\sum_{n}G_nG_n^\dagger\right) = \sum_{n,n'}G_{n'}^\dagger(G_{n'}\hat{H}G_n^\dagger)G_n, \tag{G4}$$

where $G_{n'}\hat{H}G_n^\dagger$ is a 4×4 matrix. The Hamiltonian can then be understood as a 4×4 matrix under N^2 different conditions that describe the transitions between different motional states. These individual 4×4 matrices can then be assembled into a $N\times N$ table to reduce computer memory usage in numerical computation, where N is the highest motional state we want to include in the calculation. For our calculations, we use $N = 100 \gg k_BT/\hbar\omega_r$. For a given temperature, we use the appropriate Boltzmann distribution to construct an initial-state vector, and numerical simulation is accomplished by the method described in Appendix D.

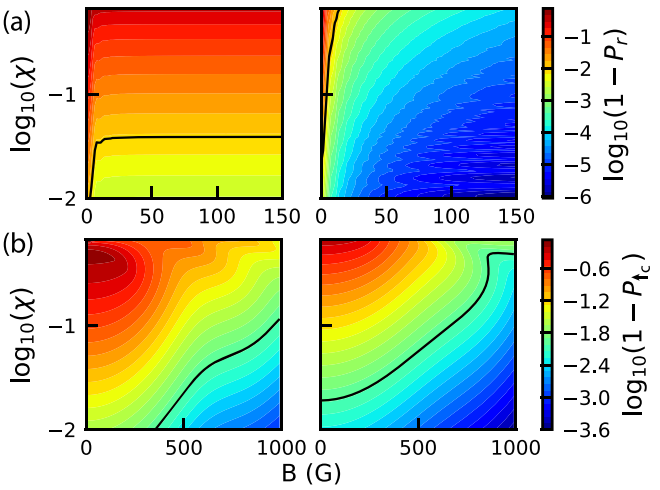

FIG. 11. Comparison of π-pulse infidelity for linearly (π) and circularly (σ^+) polarized drives. (a) Infidelity for the clock-Rydberg transition case for the linear (left) and circular (right) drive. (b) Infidelity for the ground-clock transition case for the linear (left) and circular (right) drive. The black line indicates where the infidelity crosses 0.01.

APPENDIX H: LINEARLY POLARIZED DRIVES

In this analysis, we compare the cases of driving the aforementioned transitions with linearly polarized (π) and circularly polarized (σ^+) light. The π-polarized drives target the ground-clock $|\downarrow_g\rangle \leftrightarrow |\downarrow_m\rangle$ and clock-Rydberg $|\uparrow_m\rangle \leftrightarrow |r_\uparrow\rangle$ transitions, giving $\Delta m_F = 0$ as opposed to $\Delta m_F = +1$ for the σ^+ transitions. Figure 11 shows the π-pulse infidelities for both cases, providing a direct comparison between the π and σ^+ transitions under various polarization impurities χ and magnetic field strengths B.

The π drives introduce greater sensitivity to polarization impurity, particularly for the clock-Rydberg case, because a resonant Raman condition exists between the two nuclear spin states for $\chi > 0$. In contrast, this condition does not exist for the clock-Rydberg case with σ^+ drives since the target state is stretched to maximum m_F. Hence, driving the π transition with high fidelity requires very low polarization impurity ($\chi < 10^{-2}$) and shows minimal improvement with larger magnetic fields. In contrast, σ^+ drives yield significantly greater populations in the target state $|r\rangle$ while exhibiting a much higher tolerance to impurity. Driving the four-level ground-clock transition with π polarization is also inferior to σ^+ with similar reasoning. Figure 11(b) highlights important distinctions between the drives across lower magnetic fields. We find that π-driven clock transitions with $\chi > 10^{-2}$ require larger magnetic field for the same pulse fidelity compared to the σ^+ case.

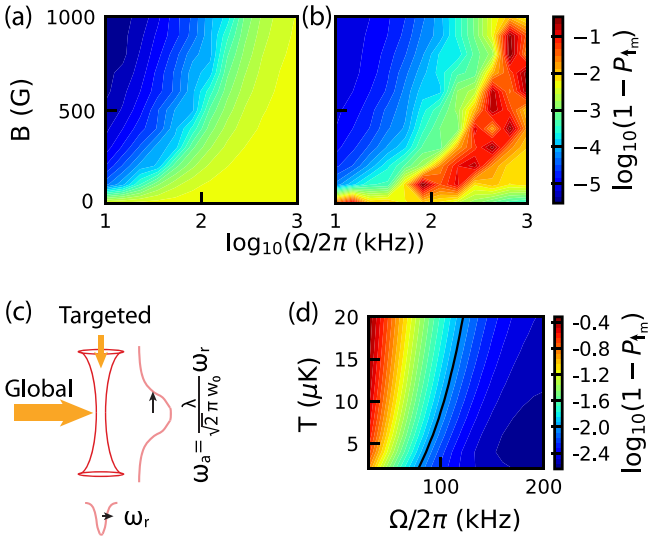

FIG. 12. Driving the clock transition for various Rabi and trap frequencies. (a) π pulse and (b) 9π pulse, initialized in $|\downarrow_g\rangle$, under various magnetic field (B) and Rabi frequency (Ω) with $\chi = 10^{-2}$. We neglect motion and thermal effects. The color scale is the population in $|\uparrow_m\rangle$, $P_{\uparrow_m}$. (b) Shows that some nonmonotonic behavior develops at high Ω due to increased coupling to the spectator states. (c) Diagram of targeted and global pulses and the corresponding relevant tweezer trapping axes. (d) The infidelity due to the finite-temperature effects for a clock beam on the axial direction.

APPENDIX I: VARYING THE CLOCK-TRANSITION RABI FREQUENCY

In the main text, we primarily consider the use of $\Omega/2\pi = 200$ kHz for the clock-transition Rabi frequency. Here, we vary Ω, neglecting motion and thermal effects, to identify conditions under which the nuclear spin splitting will limit the π-pulse fidelity and Rabi coherence time. We study the population $P_{\uparrow_m}$ in $|\uparrow_m\rangle$ after a π and 9π pulse from $|\downarrow_g\rangle$ versus magnetic field and Rabi frequency with $\chi = 10^{-2}$ (see Fig. 12). For sufficiently high Ω, the pulse fidelity after 9π is worse than that of π, which indicates the onset of non-negligible coupling to the spectator states. Interestingly, we observe nonmonotonic behavior with respect to varying Ω, which we attribute to resonance effects where the Zeeman shift of the spectator transition (which depends on B) is within the bandwidth of Ω. For higher χ this effect would become crippling even for relatively short pulses.

APPENDIX J: AXIAL ADDRESSING AND DRIVING THE CLOCK TRANSITION AT LOWER TRAP FREQUENCY

Aside from the global clock pulse, a tightly focused beam could be useful for single-qubit, mid-circuit readout. In a tweezer system, this can be accomplished by overlapping the clock laser together with a tweezer. Since a tweezer has much weaker confinement on the axial direction compared to the radial direction, the consideration of the motional states changes dramatically.

Similar to the calculation for the radial direction in Appendix G and assuming a Gaussian beam profile with fixed waist–Rayleigh length relationship, we assume an axial trap frequency in the tweezer of $\omega_z = 2\pi \times 17$ kHz [corresponding to the same tweezer parameter in the main text; see Fig. 12(c)]. Under this lower trap frequency, the simulation shown in Fig. 12(d) indicates a significantly higher fidelity for most cases when compared with the radial direction. This result can be understood by considering that an atomic transition is mostly affected by phase noise around the Rabi frequency. The atomic sloshing motion can introduce an effective phase noise around the trap frequency, which is particularly deleterious when the trap frequency is still comparable to the Rabi frequency. For the case of axial addressing, since the Rabi frequency is much higher than the trap frequency, the atom is nearly static during the clock pulse time.

However, other technical problems arise when we apply the axial driving beam, which also pertains to focused Raman-based single-qubit gates and focused Rydberg-mediated two-qubit gates [see Fig. 1(b)]. One issue is the motional stability of the tweezers and clock laser beams, which requires a relative displacement smaller than 100 nm for an intensity fluctuation smaller than 1% assuming a waist of 800 nm. This issue can be solved by adding a flat-top beam shaper, which gives a homogeneous clock laser intensity within the beam diameter. Another potential problem is the crosstalk between the target atom and its neighbors. However, considering a tweezer spacing of 2 (3) μm and an addressing beam waist radius of 800 nm, the laser Rabi crosstalk of the neighboring atoms is $\approx 10^{-3}$ ($\approx 10^{-6}$), which suggests that the operations in our architecture can exceed the 0.99 fidelity level.

Another insidious technical issue for tightly focused beams of highly constrained polarization (especially if it is circular such as the clock and Rydberg beams) is the need to maintain this polarization for all sites to be addressed by the tightly focused beams. However, this may be accomplished by carefully designing the optical system to put polarizers in the appropriate plane, perhaps combined with the use of metallic mirrors rather than dielectric mirrors. Additionally, the Pockels electro-optic effect could be used to adjust the polarization in a calibrated map via a polarimeter. Although we leave a careful study of this effect for future work, we note that trapped ion systems have been engineering solutions to such problems for over a decade [83].

APPENDIX K: TECHNICAL LIMITATIONS FOR THE RYDBERG TRANSITION

As stated above, we believe that the technical limitations of driving ground-Rydberg transitions for use in Rydberg-mediated entanglement are thoroughly described elsewhere [12,62,64], but we briefly consider them in the context of our architecture. A recurring theme is the disparate timescales between the clock drives and Rydberg drives ($\Omega_R > 10\Omega_c$), rendering the Rydberg drives less sensitive to several technical limitations.

1. Laser frequency noise

Closed-loop frequency stabilization systems introduce noise peaks, called "servo bumps," that typically span $\approx$ 100 kHz to $\approx$1 MHz. This frequency noise gives rise to a $\Delta(t)\sigma_z$ term that must be considered in addition to the

$\Omega\sigma_x$ Rabi drive term, and is well known to have particularly deleterious effects when its characteristic timescale τ matches $1/\Omega$ [12,62,64]. As described above, we consider $\Omega_c = 2\pi \times 200$ kHz for the clock transition and $\Omega_R = 2\pi \times 6$ MHz for the Rydberg transition. Therefore, the clock drive is substantially more sensitive to laser frequency noise than the Rydberg drive. Indeed, this setting for the Rydberg transition was recently used in a nearly identical system with ^{88}Sr [12], showing long-time Rabi coherence with contrast exceeding 0.99.

2. Motional and trapping effects

Unlike the clock transition for which the differential polarizability is zero at 759 nm, there is a significant differential polarizability at this wavelength for the Rydberg transition [12]. It is common to blink the traps off during Rydberg pulses. (The intended Rydberg-based gates will not leave population in the Rydberg state after the pulse.) With the atom in free flight, its motion gives rise to random Doppler shifts given by $\Delta\omega = 2\pi/\lambda\sqrt{k_B T/m}$, where λ is the optical wavelength, T is the temperature, k_B is Boltzmann's constant, and m is the mass. Assuming a temperature of 500 nK at a trap depth of 5 μK (adiabatically ramping down from a temperature of 5 μK in a 500-μK-deep trap), $\Delta\omega \approx 2\pi \times 16$ kHz. This effect is negligible compared to $\Omega_R = 2\pi \times 6$ MHz.

Alternatively, one could leave the tweezer traps on during the pulses. As discussed above, the trap frequencies in a 500-μK-deep trap are at most ≈70 kHz. While this is comparable to Ω_c, it is much smaller than Ω_R. Moreover, it is common to ramp the trap depth down by a factor of 100 bringing us to $U = 5$ μK ≈100 kHz, for which this frequency is ≈7 kHz. In this setting, $\Omega_R \gg U$. In this limit, the dominant effect from the trap is the random differential light shift due to the deviation of the atomic position from the trap bottom. Similar to the free-space case, this corresponds to $\Delta\omega \approx 2\pi \times 15$ kHz when assuming an atomic temperature of 500 nK in the 5-μK-deep trap, and assuming a relative polarizability of $\alpha_R/\alpha_c \approx -0.5$ [10,12]. The recent work with Sr [12] also studied the case with the traps on, finding minimal difference versus blinking them off.

3. Rydberg state lifetime

Here again, large Ω_R helps to mitigate the effects of decay from the Rydberg state, which again has been discussed in detail [64]. We consider the use of a Rydberg state with $n^* \approx 55$, for which we anticipate a lifetime of $\tau \approx 100$ μs. The 2π pulse of our Rydberg gates is $\tau_{2\pi} = 2\pi/\Omega_R = 167$ ns, which suggests that pulses with fidelity up to $\gtrsim$0.999 are possible when integrating over the population of the Rydberg state during the pulse. Working at cryogenic temperatures can further improve the Rydberg state lifetimes.

4. DC Stark and Zeeman effects

Finally, we consider dc drifts in the resonance frequency of the Rydberg transition originating from magnetic and electric field instability. The former is already considered in Appendix D where we assumed a 1-mG field instability and showed negligible effects, again owing to the large separation between $\Omega_R = 2\pi \times 6$ MHz and $\Delta_B = 2\pi \times 1.9$ MHz/G $\times$ 10^{-3} G $= 2\pi \times 1.9$ kHz. We do not anticipate dc Stark shifts that are significantly different than those of other atomic species with comparable n^* [12,29], and thus we do not anticipate limitations even well beyond the 0.99 level due to this effect for $n^* \approx 55$, albeit perhaps requiring interleaved line-shape measurements or active atomic locking [12,14]. In-vacuum electrode systems [10,64,84] can further suppress the effect of electric field transients, and so can operation at cryogenic temperatures.

[1] M. Saffman, T. G. Walker, and K. Mølmer, Quantum information with Rydberg atoms, Rev. Mod. Phys. **82**, 2313 (2010).

[2] A. Browaeys and T. Lahaye, Many-body physics with individually controlled Rydberg atoms, Nat. Phys. **16**, 132 (2020).

[3] M. Morgado and S. Whitlock, Quantum simulation and computing with Rydberg-interacting qubits, AVS Quantum Sci. **3**, 023501 (2021).

[4] A. Cooper, J. P. Covey, I. S. Madjarov, S. G. Porsev, M. S. Safronova, and M. Endres, Alkaline-Earth Atoms in Optical Tweezers, Phys. Rev. X **8**, 041055 (2018).

[5] M. A. Norcia, A. W. Young, and A. M. Kaufman, Microscopic Control and Detection of Ultracold Strontium in Optical-Tweezer Arrays, Phys. Rev. X **8**, 041054 (2018).

[6] S. Saskin, J. T. Wilson, B. Grinkemeyer, and J. D. Thompson, Narrow-Line Cooling and Imaging of Ytterbium Atoms in an Optical Tweezer Array, Phys. Rev. Lett. **122**, 143002 (2019).

[7] J. P. Covey, I. S. Madjarov, A. Cooper, and M. Endres, 2000-Times Repeated Imaging of Strontium Atoms in Clock-Magic Tweezer Arrays, Phys. Rev. Lett. **122**, 173201 (2019).

[8] M. A. Norcia, A. W. Young, W. J. Eckner, E. Oelker, J. Ye, and A. M. Kaufman, Seconds-scale coherence on an optical clock transition in a tweezer array, Science **366**, 93 (2019).

[9] I. S. Madjarov, A. Cooper, A. L. Shaw, J. P. Covey, V. Schkolnik, T. H. Yoon, J. R. Williams, and M. Endres, An Atomic-Array Optical Clock with Single-Atom Readout, Phys. Rev. X **9**, 041052 (2019).

[10] J. T. Wilson, S. Saskin, Y. Meng, S. Ma, R. Dilip, A. P. Burgers, and J. D. Thompson, Trapping Alkaline Earth Rydberg Atoms Optical Tweezer Arrays, Phys. Rev. Lett. **128**, 033201 (2022).

[11] N. Jackson, R. Hanley, M. Hill, F. Leroux, C. Adams, and M. Jones, Number-resolved imaging of ^{88}Sr atoms in a long working distance optical tweezer, SciPost Phys. **8**, 038 (2020).

[12] I. S. Madjarov, J. P. Covey, A. L. Shaw, J. Choi, A. Kale, A. Cooper, H. Pichler, V. Schkolnik, J. R. Williams, and M. Endres, High-fidelity entanglement and detection of alkaline-earth Rydberg atoms, Nat. Phys. **16**, 857 (2020).

[13] A. W. Young, W. J. Eckner, W. R. Milner, D. Kedar, M. A. Norcia, E. Oelker, N. Schine, J. Ye, and A. M. Kaufman, Half-minute-scale atomic coherence and high relative stability in a tweezer clock, Nature (London) **588**, 408 (2020).

[14] J. Choi, A. L. Shaw, I. S. Madjarov, X. Xie, J. P. Covey, J. S. Cotler, D. K. Mark, H.-Y. Huang, A. Kale, H. Pichler,

F. G. S. L. Brandão, S. Choi, and M. Endres, Emergent randomness and benchmarking from many-body quantum chaos, arXiv:2103.03535.

[15] A. P. Burgers, S. Ma, S. Saskin, J. Wilson, M. A. Alarcón, C. H. Greene, and J. D. Thompson, Controlling Rydberg excitations using ion core transitions in alkaline earth atom tweezer arrays, arXiv:2110.06902.

[16] N. Schine, A. W. Young, W. J. Eckner, M. J. Martin, and A. M. Kaufman, Long-lived Bell states in an array of optical clock qubits, arXiv:2111.14653.

[17] K. Barnes, P. Battaglino, B. J. Bloom, K. Cassella, R. Coxe, N. Crisosto, J. P. King, S. S. Kondov, K. Kotru, S. C. Larsen, J. Lauigan, B. J. Lester, M. McDonald, E. Megidish, S. Narayanaswami, C. Nishiguchi, R. Notermans, L. S. Peng, A. Ryou, T.-Y. Wu *et al.*, Assembly and coherent control of a register of nuclear spin qubits, Nat. Commun. **13**, 2779 (2022).

[18] A. Jenkins, J. W. Lis, A. Senoo, W. F. McGrew, and A. M. Kaufman, Ytterbium Nuclear-Spin Qubits in an Optical Tweezer Array, Phys. Rev. X **12**, 021027 (2022).

[19] S. Ma, A. P. Burgers, G. Liu, J. Wilson, B. Zhang, and J. D. Thompson, Universal Gate Operations on Nuclear Spin Qubits in an Optical Tweezer Array of ^{171}Yb Atoms, Phys. Rev. X **12**, 021028 (2022).

[20] A. D. Ludlow, M. M. Boyd, J. Ye, E. Peik, and P. O. Schmidt, Optical atomic clocks, Rev. Mod. Phys. **87**, 637 (2015).

[21] M. M. Boyd, T. Zelevinsky, A. D. Ludlow, S. Blatt, T. Zanon-Willette, S. M. Foreman, and J. Ye, Nuclear spin effects in optical lattice clocks, Phys. Rev. A **76**, 022510 (2007).

[22] J. Ye, H. J. Kimble, and H. Katori, Quantum state engineering and precision metrology using state-insensitive light traps, Science **320**, 1734 (2008).

[23] P. O. Schmidt, T. Rosenband, C. Langer, W. M. Itano, J. C. Bergquist, and D. J. Wineland, Spectroscopy using quantum logic, Science **309**, 749 (2005).

[24] L. Jiang, J. S. Hodges, J. R. Maze, P. Maurer, J. M. Taylor, D. G. Cory, P. R. Hemmer, R. L. Walsworth, A. Yacoby, A. S. Zibrov, and M. D. Lukin, Repetitive readout of a single electronic spin via quantum logic with nuclear spin ancillae, Science **326**, 267 (2009).

[25] J. J. Pla, K. Y. Tan, J. P. Dehollain, W. H. Lim, J. J. L. Morton, F. A. Zwanenburg, D. N. Jamieson, A. S. Dzurak, and A. Morello, High-fidelity readout and control of a nuclear spin qubit in silicon, Nature (London) **496**, 334 (2013).

[26] F. Arute, K. Arya, R. Babbush, D. Bacon, J. C. Bardin, R. Barends, R. Biswas, S. Boixo, F. G. S. L. Brandao, D. A. Buell, B. Burkett, Y. Chen, Z. Chen, B. Chiaro, R. Collins, W. Courtney, A. Dunsworth, E. Farhi, B. Foxen, A. Fowler *et al.*, Quantum supremacy using a programmable superconducting processor, Nature (London) **574**, 505 (2019).

[27] K. Singh, S. Anand, A. Pocklington, J. T. Kemp, and H. Bernien, Dual-Element, Two-Dimensional Atom Array with Continuous-Mode Operation, Phys. Rev. X **12**, 011040 (2022).

[28] D. T. C. Allcock, W. C. Campbell, J. Chiaverini, I. L. Chuang, E. R. Hudson, I. D. Moore, A. Ransford, C. Roman, J. M. Sage, and D. J. Wineland, omg blueprint for trapped ion quantum computing with metastable states, Appl. Phys. Lett. **119**, 214002 (2021).

[29] H. Levine, A. Keesling, G. Semeghini, A. Omran, T. T. Wang, S. Ebadi, H. Bernien, M. Greiner, V. Vuletić, H. Pichler, and M. D. Lukin, Parallel Implementation of High-Fidelity Multiqubit Gates with Neutral Atoms, Phys. Rev. Lett. **123**, 170503 (2019).

[30] E. Knill, Quantum computing with realistically noisy devices, Nature (London) **434**, 39 (2005).

[31] A. G. Fowler, M. Mariantoni, J. M. Martinis, and A. N. Cleland, Surface codes: Towards practical large-scale quantum computation, Phys. Rev. A **86**, 032324 (2012).

[32] A. J. Daley, M. M. Boyd, J. Ye, and P. Zoller, Quantum Computing with Alkaline-Earth-Metal Atoms, Phys. Rev. Lett. **101**, 170504 (2008).

[33] A. V. Gorshkov, A. M. Rey, A. J. Daley, M. M. Boyd, J. Ye, P. Zoller, and M. D. Lukin, Alkaline-Earth-Metal Atoms as Few-Qubit Quantum Registers, Phys. Rev. Lett. **102**, 110503 (2009).

[34] A. V. Gorshkov, M. Hermele, V. Gurarie, C. Xu, P. S. Julienne, J. Ye, P. Zoller, E. Demler, M. D. Lukin, and A. M. Rey, Two-orbital S U(N) magnetism with ultracold alkaline-earth atoms, Nat. Phys. **6**, 289 (2010).

[35] G. Pagano, F. Scazza, and M. Foss-Feig, Fast and scalable quantum information processing with two-electron atoms in optical tweezer arrays, Adv. Quantum Technol. **2**, 1800067 (2019).

[36] I. Cong, S.-T. Wang, H. Levine, A. Keesling, and M. D. Lukin, Hardware-efficient, fault-tolerant quantum computation with rydberg atoms, arXiv:2105.13501.

[37] J. P. Covey, A. Sipahigil, S. Szoke, N. Sinclair, M. Endres, and O. Painter, Telecom-Band Quantum Optics with Ytterbium Atoms and Silicon Nanophotonics, Phys. Rev. Appl. **11**, 034044 (2019).

[38] W. Huie, S. G. Menon, H. Bernien, and J. P. Covey, Multiplexed telecommunication-band quantum networking with atom arrays in optical cavities, Phys. Rev. Research **3**, 043154 (2021).

[39] L. I. R. Gil, R. Mukherjee, E. M. Bridge, M. P. A. Jones, and T. Pohl, Spin Squeezing in a Rydberg Lattice Clock, Phys. Rev. Lett. **112**, 103601 (2014).

[40] E. M. Kessler, P. Kómár, M. Bishof, L. Jiang, A. S. Sørensen, J. Ye, and M. D. Lukin, Heisenberg-Limited Atom Clocks Based on Entangled Qubits, Phys. Rev. Lett. **112**, 190403 (2014).

[41] R. Kaubruegger, P. Silvi, C. Kokail, R. van Bijnen, A. M. Rey, J. Ye, A. M. Kaufman, and P. Zoller, Variational Spin-Squeezing Algorithms on Programmable Quantum Sensors, Phys. Rev. Lett. **123**, 260505 (2019).

[42] T. Monz, D. Nigg, E. A. Martinez, M. F. Brandl, P. Schindler, R. Rines, S. X. Wang, I. L. Chuang, and R. Blatt, Realization of a scalable Shor algorithm, Science **351**, 1068 (2016).

[43] A. Erhard, H. Poulsen Nautrup, M. Meth, L. Postler, R. Stricker, M. Stadler, V. Negnevitsky, M. Ringbauer, P. Schindler, H. J. Briegel, R. Blatt, N. Friis, and T. Monz, Entangling logical qubits with lattice surgery, Nature (London) **589**, 220 (2021).

[44] T. M. Graham, Y. Song, J. Scott, C. Poole, L. Phuttitarn, K. Jooya, P. Eichler, X. Jiang, A. Marra, B. Grinkemeyer, M. Kwon, M. Ebert, J. Cherek, M. T. Lichtman, M. Gillette, J. Gilbert, D. Bowman, T. Ballance, C. Campbell, E. D. Dahl *et al.*, Multi-qubit entanglement and algorithms on a neutral-atom quantum computer, Nature (London) **604**, 457 (2022).

[45] A. Lengwenus, J. Kruse, M. Schlosser, S. Tichelmann, and G. Birkl, Coherent Transport of Atomic Quantum States

in a Scalable Shift Register, Phys. Rev. Lett. **105**, 170502 (2010).

[46] T. Đorđević, P. Samutpraphoot, P. L. Ocola, H. Bernien, B. Grinkemeyer, I. Dimitrova, V. Vuletić, and M. D. Lukin, Entanglement transport and a nanophotonic interface for atoms in optical tweezers, Science **373**, 1511 (2021).

[47] D. Bluvstein, H. Levine, G. Semeghini, T. T. Wang, S. Ebadi, M. Kalinowski, A. Keesling, N. Maskara, H. Pichler, M. Greiner, V. Vuletić, and M. D. Lukin, A quantum processor based on coherent transport of entangled atom arrays, Nature (London) **604**, 451 (2022).

[48] J. Chiaverini, D. Leibfried, T. Schaetz, M. D. Barrett, R. B. Blakestad, J. Britton, W. M. Itano, J. D. Jost, E. Knill, C. Langer, R. Ozeri, and D. J. Wineland, Realization of quantum error correction, Nature (London) **432**, 602 (2004).

[49] T. Schaetz, M. D. Barrett, D. Leibfried, J. Chiaverini, J. Britton, W. M. Itano, J. D. Jost, C. Langer, and D. J. Wineland, Quantum Dense Coding with Atomic Qubits, Phys. Rev. Lett. **93**, 040505 (2004).

[50] M. Endres, H. Bernien, A. Keesling, H. Levine, E. R. Anschuetz, A. Krajenbrink, C. Senko, V. Vuletic, M. Greiner, and M. D. Lukin, Atom-by-atom assembly of defect-free one-dimensional cold atom arrays, Science **354**, 1024 (2016).

[51] X.-F. Shi, Rydberg quantum computation with nuclear spins in two-electron neutral atoms, Front. Phys. **16**, 52501 (2021).

[52] T. M. Graham, M. Kwon, B. Grinkemeyer, Z. Marra, X. Jiang, M. T. Lichtman, Y. Sun, M. Ebert, and M. Saffman, Rydberg-Mediated Entanglement in a Two-Dimensional Neutral Atom Qubit Array, Phys. Rev. Lett. **123**, 230501 (2019).

[53] F. Robicheaux, D. W. Booth, and M. Saffman, Theory of long-range interactions for Rydberg states attached to hyperfine-split cores, Phys. Rev. A **97**, 022508 (2018).

[54] R. Ding, J. D. Whalen, S. K. Kanungo, T. C. Killian, F. B. Dunning, S. Yoshida, and J. Burgdörfer, Spectroscopy of Sr-87 triplet Rydberg states, Phys. Rev. A **98**, 042505 (2018).

[55] F. Robicheaux, Calculations of long range interactions for 87 Sr Rydberg states, J. Phys. B: At., Mol. Opt. Phys. **52**, 244001 (2019).

[56] M. Aymar, C. H. Greene, and E. Luc-Koenig, Multichannel Rydberg spectroscopy of complex atoms, Rev. Mod. Phys. **68**, 1015 (1996).

[57] R. W. Berends and L. Maleki, Hyperfine structure and isotope shifts of transitions in neutral and singly ionized ytterbium, J. Opt. Soc. Am. B **9**, 332 (1992).

[58] K. T. Lu and U. Fano, Graphic analysis of perturbed rydberg series, Phys. Rev. A **2**, 81 (1970).

[59] S. A. Moses, J. P. Covey, M. T. Miecnikowski, B. Yan, B. Gadway, J. Ye, and D. S. Jin, Creation of a low-entropy quantum gas of polar molecules in an optical lattice, Science **350**, 659 (2015).

[60] J. P. Covey, S. A. Moses, M. Gärttner, A. Safavi-Naini, M. T. Miecnikowski, Z. Fu, J. Schachenmayer, P. S. Julienne, A. M. Rey, D. S. Jin, and J. Ye, Doublon dynamics and polar molecule production in an optical lattice, Nat. Commun. **7**, 11279 (2016).

[61] M. J. Martin, Y.-Y. Jau, J. Lee, A. Mitra, I. H. Deutsch, and G. W. Biedermann, A mølmer-sørensen gate with rydberg-dressed atoms, arXiv:2111.14677.

[62] H. Levine, A. Keesling, A. Omran, H. Bernien, S. Schwartz, A. S. Zibrov, M. Endres, M. Greiner, V. Vuletić, and M. D. Lukin, High-Fidelity Control and Entanglement of Rydberg-Atom Qubits, Phys. Rev. Lett. **121**, 123603 (2018).

[63] H. Bernien, S. Schwartz, A. Keesling, H. Levine, A. Omran, H. Pichler, S. Choi, A. S. Zibrov, M. Endres, M. Greiner, V. Vuletić, and M. D. Lukin, Probing many-body dynamics on a 51-atom quantum simulator, Nature (London) **551**, 579 (2017).

[64] S. de Léséleuc, D. Barredo, V. Lienhard, A. Browaeys, and T. Lahaye, Analysis of imperfections in the coherent optical excitation of single atoms to Rydberg states, Phys. Rev. A **97**, 053803 (2018).

[65] T. Hong, C. Cramer, E. Cook, W. Nagourney, and E. N. Fortson, Observation of the $^1S_0$ - $^3P_0$ transition in atomic ytterbium for optical clocks and qubit arrays, Opt. Lett. **30**, 2644 (2005).

[66] A. Kale, Towards high fidelity quantum computation and simulation with rydberg atoms, B.S. thesis, California Institute of Technology, 2020.

[67] F. Scazza, C. Hofrichter, M. Höfer, P. C. De Groot, I. Bloch, and S. Fölling, Observation of two-orbital spin-exchange interactions with ultracold SU(N)-symmetric fermions, Nat. Phys. **10**, 779 (2014).

[68] S. Omanakuttan, A. Mitra, M. J. Martin, and I. H. Deutsch, Quantum optimal control of nuclear spin qudecimals in ^{87}Sr, arXiv:2106.13705.

[69] V. V. Albert, J. P. Covey, and J. Preskill, Robust Encoding of a Qubit in a Molecule, Phys. Rev. X **10**, 031050 (2020).

[70] H. X. Yang, J. Y. Ma, Y. K. Wu, Y. Wang, M. M. Cao, W. X. Guo, Y. Y. Huang, L. Feng, Z. C. Zhou, and L. M. Duan, Realizing coherently convertible dual-type qubits with the same ion species, arXiv:2106.14906.

[71] Y. Wu, S. Kolkowitz, S. Puri, and J. D. Thompson, Erasure conversion for fault-tolerant quantum computing in alkaline earth Rydberg atom arrays, arXiv:2201.03540.

[72] U. Fano, Quantum Defect Theory of l Uncoupling in H_2 as an example of channel-interaction treatment, Phys. Rev. A **2**, 353 (1970).

[73] C.-M. Lee and K. T. Lu, Spectroscopy and collision theory. II. The Ar absorption spectrum, Phys. Rev. A **8**, 1241 (1973).

[74] J.-Q. Sun and K. T. Lu, Hyperfine structure of extremely high Rydberg msns $^1S_0$ and msns $^3S_1$ series in odd alkaline-earth isotopes, J. Phys. B: At., Mol. Opt. Phys. **21**, 1957 (1988).

[75] J.-Q. Sun, Multichannel quantum defect theory of the hyperfine structure of high Rydberg states, Phys. Rev. A **40**, 7355 (1989).

[76] H. Lehec, A. Zuliani, W. Maineult, E. Luc-Koenig, P. Pillet, P. Cheinet, F. Niyaz, and T. F. Gallagher, Laser and microwave spectroscopy of even-parity Rydberg states of neutral ytterbium and multichannel-quantum-defect-theory analysis, Phys. Rev. A **98**, 062506 (2018).

[77] E. Robertson, N. Šibalić, R. Potvliege, and M. Jones, ARC 3.0: An expanded Python toolbox for atomic physics calculations, Comput. Phys. Commun. **261**, 107814 (2021).

[78] N. D. Lemke, Optical lattice clock with spin-1/2 ytterbium atoms, Ph.D. thesis, University of Colorado-Boulder, 2012.

[79] W. H. Press, S. A. Teukolsky, W. T. Vetterling, and B. P. Flannery, *Numerical Recipes 3rd Edition: The Art of Scientific Computing*, 3rd ed. (Cambridge University Press, New York, 2007).

[80] K. Beloy, J. A. Sherman, N. D. Lemke, N. Hinkley, C. W. Oates, and A. D. Ludlow, Determination of the $5d6s\,^3D_1$ state lifetime and blackbody radiation clock shift in Yb, Phys. Rev. A **86**, 051404(R) (2012).

[81] M. G. Tarallo, Development of a strontium optical lattice clock, Ph.D. thesis, University of Pisa, 2009.

[82] G. Di Domenico, S. Schilt, and P. Thomann, Simple approach to the relation between laser frequency noise and laser line shape, Appl. Opt. **49**, 4801 (2010).

[83] D. Leibfried, R. Blatt, C. Monroe, and D. Wineland, Quantum dynamics of single trapped ions, Rev. Mod. Phys. **75**, 281 (2003).

[84] J. P. Covey, *Enhanced Optical and Electric Manipulation of a Quantum Gas of KRb Molecules*, Springer Theses (Springer, Cham, 2018).